# The July Climate and a Comparison of the January and July Climates Simulated by the GISS General Circulation Model

P. H. STONE,[1] S. CHOW[2] AND W. J. QUIRK

*Institute for Space Studies, Goddard Space Flight Center, NASA, New York, N. Y. 10025*

## ABSTRACT

The GISS global general circulation model has been used to simulate July conditions, in a manner analogous to the previously described January simulation. Sea surface temperatures, ice cover, snow line and soil moisture were assigned values based on climatological data for July, and the integration was started from real data for 18 June 1973. Because of the realistic initial condition, the model rapidly approached a quasi-steady state. Mean statistics were computed for the simulated calendar month of July, and compared with climatological data, mainly for the Northern Hemisphere troposphere. Qualitatively, the model-generated energy cycle, distributions of winds, temperature, humidity and pressure, dynamical transports, diabatic heating, evaporation, precipitation and cloud cover are all realistic. Quantitatively, the July simulation, like the January simulation, tends to underestimate the strength of the mean meridional circulations, the eddy activity and some of the associated transports. The July simulation of zonal mean temperature and zonal wind fields is superior to the January simulation in the Northern Hemisphere because of the absence of the polar night jet, and the decreased importance of large-scale dynamical heating and cooling in summer.

In order to assess the model's ability to simulate seasonal differences, the July and January simulations were compared with each other and with climatological data on seasonal changes. The model simulates accurately the northward displacement of the mid-latitude jets, the low-latitude Hadley cells, the tropical rain belt, the trade winds, and the ITCZ in July compared to January, the reversal of the Indian monsoon, and the weakening of the zonal meridional circulations and the decline of eddy activity in the summer. The simulated seasonal differences in the Southern Hemisphere are much less pronounced than in the Northern Hemisphere as expected.

From a climatological point of view, there are three particular aspects of the model's simulations that need to be improved: 1) arctic regions in January are as much as 10°K too cold, because of the model's underestimate of the dynamical transports of heat into high latitudes; 2) the simulation of the climatological fields in the vicinity of the Himalayas and Southeast Asia is noticeably poorer than in other areas—for example, in Southeast Asia in the July simulation the rainfall is half the observed amount; and 3) the global albedo in July is too high when compared to satellite-derived values (0.35 vs 0.26), at least partially because the model-simulated deep, penetrating cumulus clouds occur too frequently in July.

## 1. Introduction

The global general circulation model (GCM) of the Goddard Institute for Space Studies (GISS) was developed originally for use in observing system simulation experiments, asynoptic data assimilation studies and experimental forecasting (Jastrow and Halem, 1973). Previous tests of the model's skill have been designed with these uses in mind (Somerville *et al.*, 1974; Druyan, 1974; Tennenbaum, 1976; Druyan *et al.*, 1975). These tests have shown that the model's skill at simulating tropospheric statistics and forecasting weather in the Northern Hemisphere in winter is comparable to that of other GCM's with similar resolution.

More recently, the GISS model has been used in climate sensitivity studies (Charney *et al.*, 1975; Somerville *et al.*, 1976). Validation of any GCM for use in such studies requires somewhat different tests of its skill from those referred to above. Ideally one would like to demonstrate that the model can simulate accurately an observed *change* in climate. The one change for which good observations are available is the seasonal change from winter to summer, which is in fact just a climate change on a short time scale. Since the seasonal changes are substantial, they represent a simple, stringent test for validating any climate model developed without reference to observed seasonal changes.

Tests of the ability of other GCM's to simulate the atmosphere have also concentrated on simulations of winter conditions (Holloway and Manabe, 1971; Kasahara *et al.*, 1973; Newson, 1974; Gates, 1975).

[1] Current affiliation: Department of Meteorology, Massachusetts Institute of Technology, Cambridge 02139.

[2] GTE Information Systems, 2880 Broadway, New York, N. Y. 10025.

TABLE 2.1. Properties of clouds in the GISS model.

| Cloud type | Layers | Analogy | Optical thickness | Albedo |
|---|---|---|---|---|
| Supersaturation | 2 | Ci | 1 | 0.12 |
| Supersaturation | 3 | Ci | 2 | 0.21 |
| Supersaturation | 4 | As | 4 | 0.34 |
| Supersaturation | 5 or 6 | As | 6 | 0.44 |
| Supersaturation | 7 or 8 or 9 | St | 8 | 0.51 |
| Penetrating convection | 4–7 or 5–8 or 6–9 | Cb | 32 | 0.81 |
| Mid-level convection | 5 or 6 | Ac | 8 | 0.51 |
| Low-level convection | 7 or 8 | Cu | 16 | 0.68 |

Current GCM's generally prescribe boundary conditions such as sea-surface temperature, but this does not prevent one from testing their ability to simulate seasonal differences in atmospheric processes that accompany prescribed seasonal differences in boundary conditions. The skill of a GCM in simulating some aspects of seasonal change has been studied by Manabe et al. (1974) and Manabe and Holloway (1975). These studies were concerned with seasonal changes in the tropics and in the hydrological cycle, respectively. However, no study of the skill of a GCM in simulating, for example, seasonal differences in the hemispheric heat balance or energetics, or in the polar heat balance, has been published. Polar conditions are particularly crucial in climate problems (SMIC, 1971), and many simplified climate models have been based solely on the heat balance (Sellers, 1969; Budyko, 1969; Gal-Chen and Schneider, 1976).

Consequently, in this paper we present a study of the skill of the GISS GCM in simulating seasonal differences. In Section 2 we give a brief description of the model. More details can be found in Somerville et al. (1974). In Section 3 we describe the results of an experiment simulating the July climatology which parallels the January simulation presented by Somerville et al. (1974). In Section 4 we directly compare the January and July simulations with each other and with observations. Finally, we summarize our results in Section 5. More details of the simulated July climatology and January–July differences are included in a technical report available from the Institute for Space Studies.

## 2. Model description

The GISS model is a global, primitive equation model, with longitude and latitude as horizontal coordinates, and a vertical sigma coordinate defined by

$$\sigma = \frac{P - P_t}{P_s - P_t},$$

where $P$ is the pressure, $P_s$ the surface pressure and $P_t$ the pressure at the top of the model atmosphere, taken to be 10 mb. Integrations are performed with nine equally spaced levels in the vertical, a horizontal grid of 4° of latitude by 5° of longitude, and a time step of 5 min. The numerical method of integration is that given by Arakawa (1972) for a distribution of variables over the horizontal grid corresponding to his Scheme B. The space-differencing is quasi-conservative for enstrophy and kinetic energy, and the time-differencing is a combination of the regular Matsuno and the time-alternating space-uncentered Matsuno procedures.

The model contains no explicit subgrid-scale horizontal diffusion. Subgrid-scale vertical diffusion is
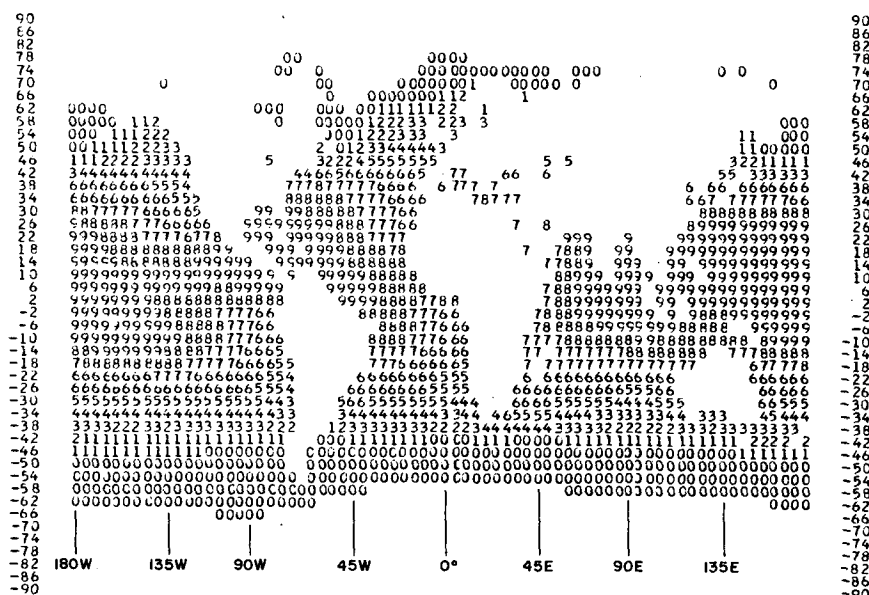


FIG. 2.1. Sea surface temperature field for July. Legend: (0) 0–9°C; (1) 9–11°C; (2) 11–13°C; (3) 13–15°C; (4) 15–17°C; (5) 17–19°C; (6) 19–23°C; (7) 23–25°C; (8) 25–27°C; (9) above 27°C.
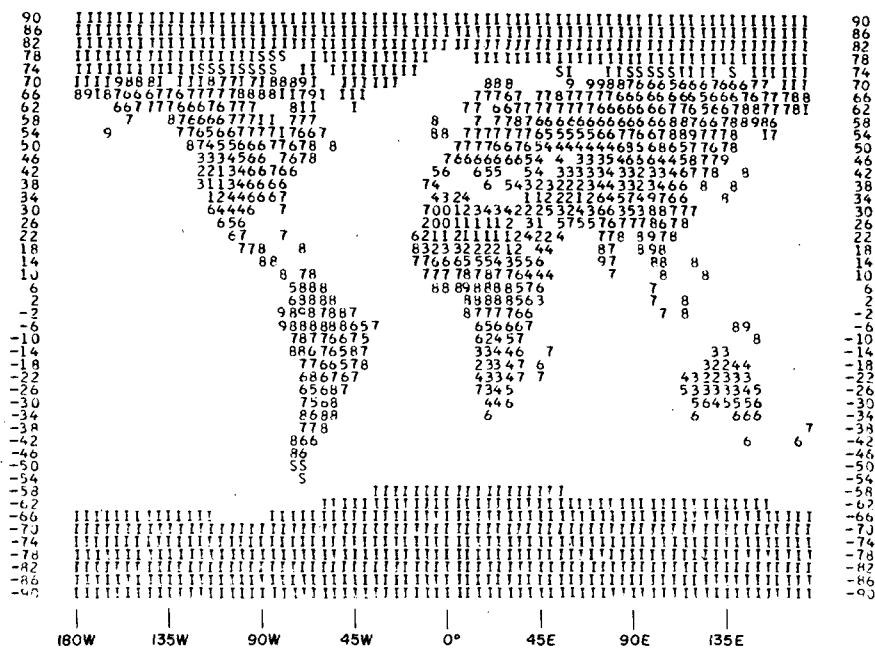
FIG. 2.2. Global distribution of snow on 1 July (S) and of ice (I) and ground wetness (percent of saturation) for July. Legend: (0) 0–5%; (1) 5–15%; (2) 15–25%; (3) 25–35%, (4) 35–45%; (5) 45–55%; (6) 55–65%; (7) 65–75%; (8) 75–85%, (9) 85–100%.

included by means of diffusion laws with simple parameterizations for the kinematic eddy viscosity, thermal diffusivity and water-vapor diffusivity based on Deardorff's (1967) work and on experiments with the GISS model (Stone et al., 1974). The only difference between the model used in the calculations and comparisons reported here, and that used in the calculations reported earlier by Somerville et al. (1974), is in the calculation of the eddy diffusion coefficients in the lowest model layer. In particular, these coefficients depend on the static stability of the lowest model layer [see Eq. (12) of Somerville et al. (1974)], and the method of calculating this static stability has been changed. The difference formula for this quantity in the earlier calculations used the ground temperature, while in the present-calculations the ground temperature was replaced by the surface air temperature. The January simulation described by Somerville et al. (1974) was repeated with this modified formula, in order to provide an unambiguous comparison with the July simulation described in Section 3.

The diabatic heating includes contributions from radiation, condensation and convection as well as from diffusion. The absorption of solar radiation is parameterized with formulas based on detailed multiple scattering calculations (Lacis and Hansen, 1974). The amount of absorption depends on the model-generated clouds and humidity, and varies with the solar zenith angle and the solar flux. The solar zenith angle and flux are calculated from the earth's orbital elements, and change diurnally and seasonally. Longwave radiative heating rates are calculated from simplified nongray calcula-

tions using twice the number of model layers, and are dependent on the model-generated clouds, temperature and humidity.

Condensation in the model is generated by two different mechanisms, large-scale supersaturation and small-scale moist convection. Supersaturation occurs whenever the relative humidity exceeds 100%, and moist convection whenever the moist static energy at lower atmospheric levels exceeds the saturated moist static energy at higher levels. The diabatic heating due to large-scale supersaturation is calculated by assuming that condensation reduces the relative humidity of the supersaturated levels to 100%, and that the condensed water either reevaporates in the next lower layers or precipitates to the ground if all lower layers are saturated. The heating due to moist convection is parameterized by Arakawa's scheme for moist convection in a 3-layer model (Arakawa et al., 1969) adapted to a 9-layer model. In this scheme the atmosphere is heated by the subsidence generated by the upward mass flux in the convective clouds, and humidity in excess of saturation in any layer condenses and precipitates, directly to the ground in the case of deep or middle level convection or to the next lowest unsaturated layer in the case of low-level convection. These are, of course, gross simplifications of the actual processes. Dry convection is also included by means of a conventional adiabatic adjustment scheme.

Clouds are generated whenever large-scale supersaturation or small-scale moist convection occurs. Table 2.1 lists the eight cloud types and subtypes which may be generated, depending on the initiating
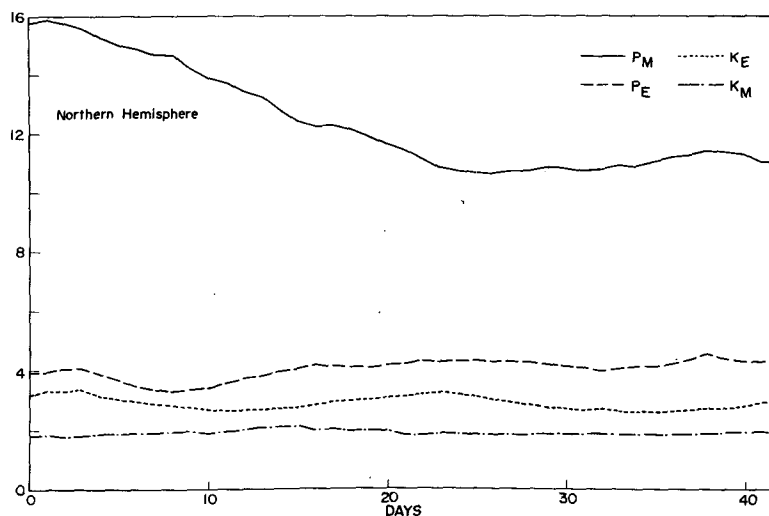
FIG. 3.1. Time evolution between 18 June and 31 July in the Northern Hemisphere model troposphere (layers 2–9) of the integrated zonal available potential energy $(P_M)$, eddy available potential energy $(P_E)$, eddy kinetic energy $(K_E)$, and zonal kinetic energy $(K_M)$. Units: $10^5$ J m$^{-2}$.

process and the atmospheric layers affected. For each cloud type the table lists the layers in which they occur (the model's layers are numbered from one to nine from top to bottom), the most closely analogous atmospheric cloud type; the cloud's shortwave optical thickness, and its visual albedo. The optical thickness $\tau$ is based on observations of the analogous cloud types, and the albedos $a$ are calculated from an approximate formula derived from scattering theory by Lacis and Hansen (1974):

$$a = \frac{0.13\tau}{1+0.13\tau}.$$

For purposes of calculating longwave heating rates, all clouds are treated as blackbodies.

Ground temperatures are predicted from the net heating and cooling at the surface by radiation, sensible heat and latent heat fluxes. Sea-surface temperatures are prescribed, and Fig. 2.1 shows the values used in the July simulation. These sea-surface temperatures were taken from Schutz and Gates' (1972b) July analysis, which is based on data from Washington and Thiel (1970) and from the U. S. Navy Hydrographic Office Atlases (1944, 1957, 1958). The surface fluxes of sensible and latent heat and the surface stress are parameterized by drag laws. The surface albedo is
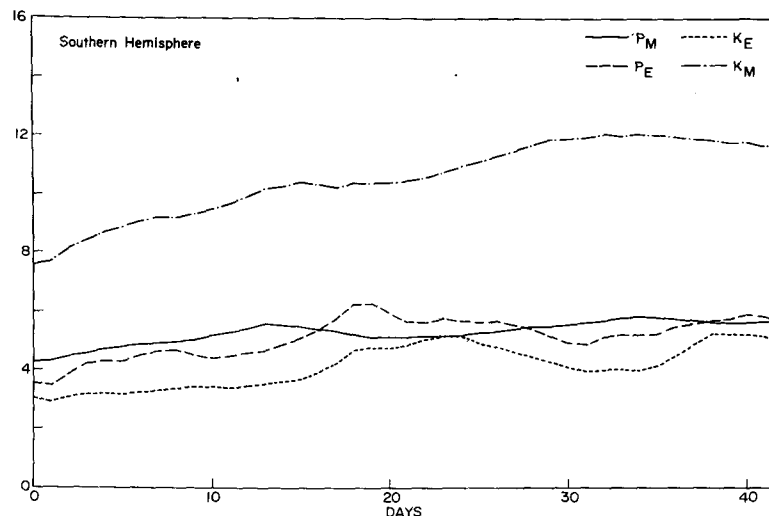


FIG. 3.2. As in Fig. 3.1 execpt for the Southern Hemisphere and the units of $P_M$ have been changed to $10^6$ J m$^{-2}$.
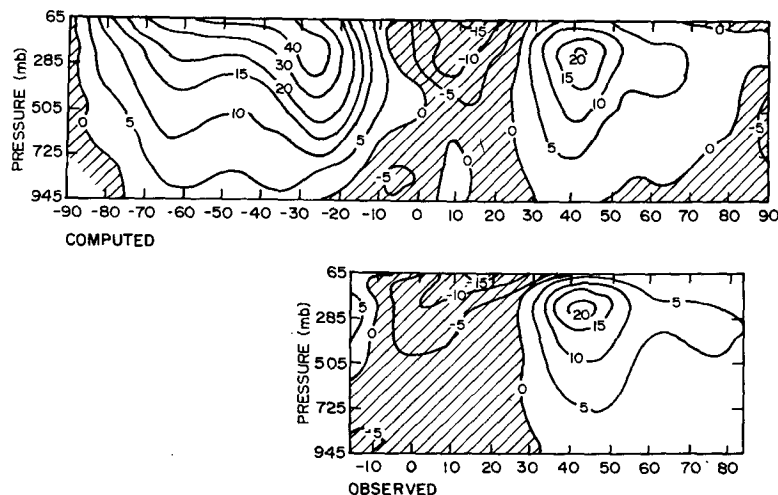
FIG. 3.3. Computed and observed July zonal mean fields of zonal wind. Observed field is based on data from Oort and Rasmusson (1971). Units: m s$^{-1}$. Negative (easterly) winds are shaded.

taken to be 0.07 over water, 0.14 over land and 0.7 over ice and snow. The distribution of ice used in the July simulation is shown in Fig. 2.2. This distribution was also taken from Schutz and Gates (1972b). The snow line over land varies daily according to Eq. (11) given by Somerville et al. (1974). The ground wetness GW (percent of saturation) used in the calculation of latent heat fluxes at the surface is fixed, and is calculated for each grid point over land from observed mean surface relative humidities, SRH, by using the ad hoc formula

$$GW = \frac{SRH - 15}{85}.$$

The surface relative humidities used in this calculation were those given by Gates (1972), which were based on data from Crutcher and Meserve (1970) and

Taljaard et al. (1969). The resulting values of ground wetness for July are also given in Fig. 2.2. Grid points with ice, snow or ocean are assumed to have a ground wetness of 100%. The ground has a smoothed but otherwise realistic topography, illustrated in Fig. 4 of Somerville et al. (1974). The boundary conditions used in the January simulations are given by Somerville et al. (1974).

3. July simulation

The July simulation was carried out in a way exactly analogous to the January simulation. The integration was started from an initial state taken from real data, in this case data for 18 June 1973, supplied by the National Meteorological Center (NMC) in Washington, D.C. (The January integration started from real data for 20 December 1972). The data were taken from
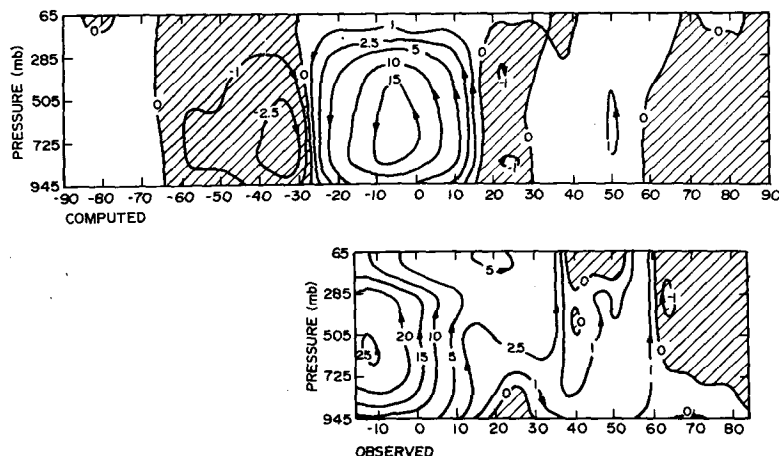


FIG. 3.4. Computed and observed streamlines of the July mean meridional circulation. Observed field is based on data from Oort and Rasmusson (1971). Units: 10$^{10}$ kg s$^{-1}$. Negative regions are shaded.
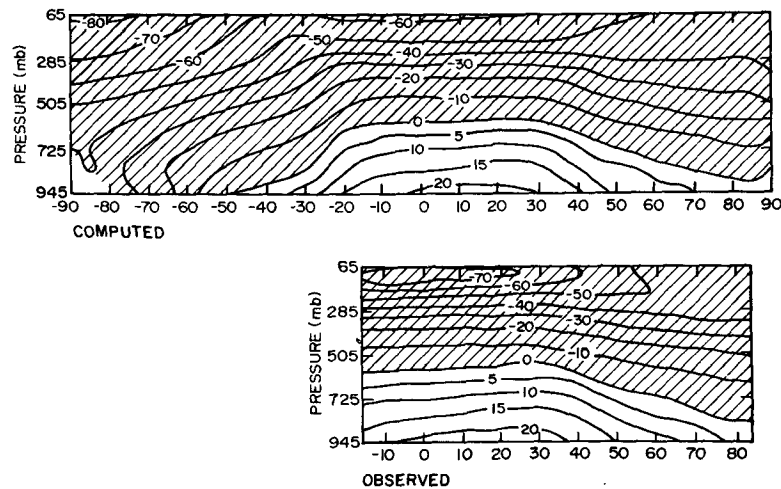
FIG. 3.5. Computed and observed July zonal mean fields of temperature. Observed field is based on data from Oort and Rasmusson (1971). Units: °C. Negative regions are shaded.

NMC's experimental global data set (Flattery, 1971). These data did not include humidities for the model's upper three layers, so climatological values were used for these humidities. The sea-surface temperature, ice cover and soil moisture throughout the integration were fixed at the July mean climatological values given in Section 2. Solar declination, solar insolation and snow line varied with calendar date as described in Section 2.

*a. Time evolution*

The integration was carried out for 44 days of simulated time, through 31 July. Figs. 3.1 and 3.2 show the computed time evolution in the Northern and Southern Hemispheres, respectively, of the integrated tropospheric (layers 2–9) zonal kinetic energy $(K_M)$, eddy kinetic energy $(K_E)$, zonal available potential energy $(P_M)$ and eddy available potential energy $(P_E)$. Be-

cause of the realistic initial state the integration approached a quasi-equilibrium state within one or two weeks. The longer term changes in $P_M$ in the Northern Hemisphere and in $K_M$ in the Southern Hemisphere during the integration are seasonal changes, and are realistic. For example, Peixoto and Oort (1974) found that in the Northern Hemisphere the monthly mean value of $P_M$ changed from $18.8 \times 10^5$ J m$^{-2}$ in June to $13.0 \times 10^5$ J m$^{-2}$ in July; a similar change is apparent in Fig. 3.1.

In addition, smaller amplitude fluctuations occur, especially in eddy energies in the Southern Hemisphere. These fluctuations have the same properties as the vacillations found in the Southern Hemisphere Eole balloon data by Webster and Keller (1975). For example, the fluctuations have about a 20-day period, and the changes in the eddy and zonal kinetic energies
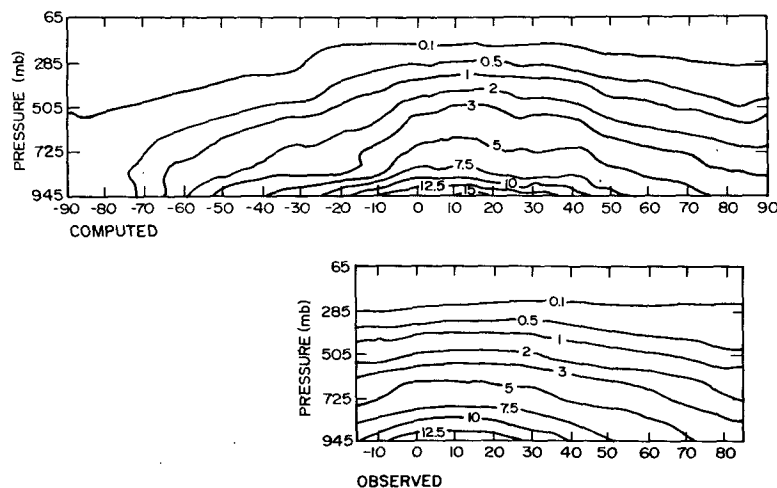


FIG. 3.6. Computed and observed July zonal mean fields of specific humidity. Observed field is based on data from Oort and Rasmusson (1971). Units: g kg$^{-1}$.
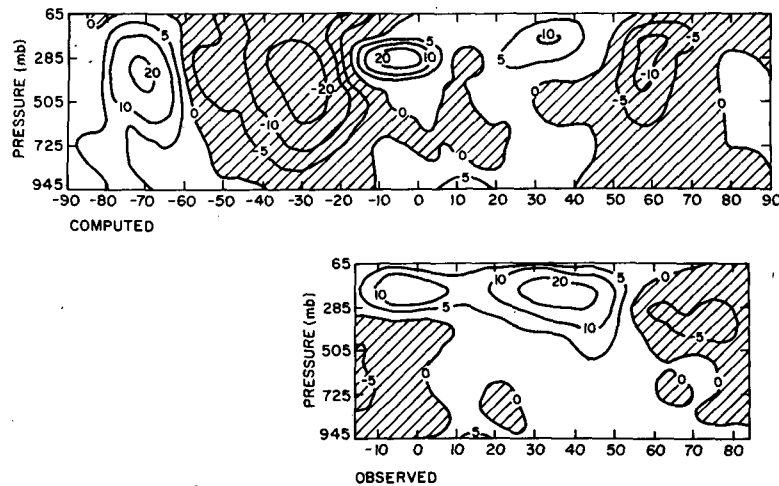
FIG. 3.7. Computed and observed July zonal mean fields of northward transport of westerly momentum by eddies. Observed field is based on data from Oort and Rasmusson (1971). Units: m² s⁻². Negative regions are shaded.

are negatively correlated in accord with Webster and Keller's findings. This vacillation is also apparent in the January simulation of the Southern Hemisphere (Somerville et al., 1974, Fig. 10). There is just a hint of a similar vacillation in the Northern Hemisphere energies, but if it is real, it is much less pronounced than in the Southern Hemisphere in both the winter and summer seasons. An experiment in which the subgrid-scale eddy viscosity was completely suppressed shows this same sort of vacillation more prominently in the Northern Hemisphere (Stone et al., 1974). This suggests that the greater prominence of the vacillation in the Southern Hemisphere is due to a smaller effective viscosity in the Southern Hemisphere, perhaps because of the lesser prominence of mountains in the Southern Hemisphere. The simulated energy cycle is discussed in Section 4a.

b. Zonal mean state

Figs. 3.3 and 3.4 show the simulated zonal mean wind fields, along with the observed zonal mean wind fields in the Northern Hemisphere based on data from Oort and Rasmusson (1971). The Southern Hemisphere observations of mean zonal motions are given by van Loon (1972). The simulated mean zonal motions (Fig. 3.3) are in excellent agreement with the observations in both hemispheres. In fact the July simulation of zonal winds in the Northern Hemisphere is superior to the January simulation, mainly because the model's resolution in the stratosphere is inadequate for resolving the Northern Hemisphere's polar night jet (Somerville et al., 1974). The streamfunction for the mean meridional circulations (Fig. 3.4) is simulated well qualitatively, i.e., the strong Southern Hemisphere Hadley
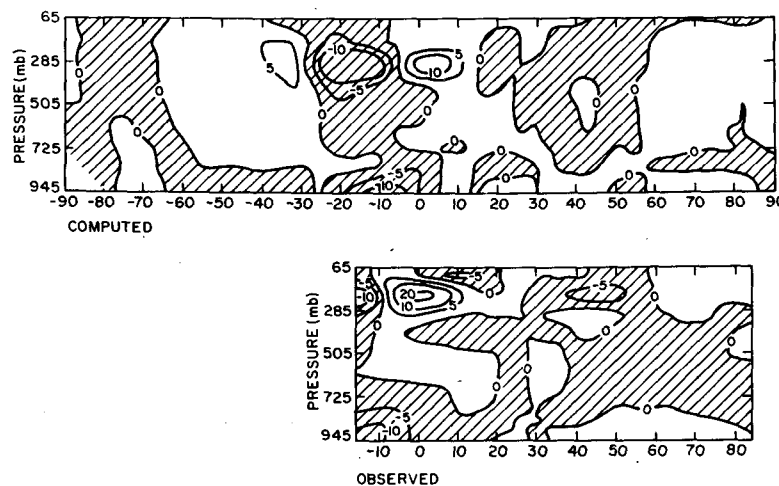


FIG. 3.8. As in Fig. 3.7 except for northward transport of westerly momentum by the mean meridional circulations.
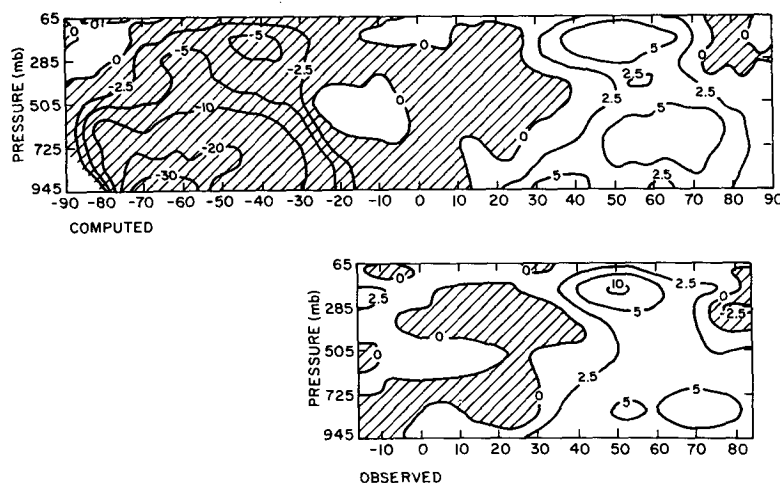
FIG. 3.9. As in Fig. 3.7 except for northward transport of sensible heat by eddies.
Units: °C m s⁻¹.

cell and the weak Northern Hemisphere Hadley and Ferrel cells are all reproduced in the simulations in about the right locations. However, the meridional circulations in the simulation are underestimated compared to the observations. Similar underestimates occurred in the January simulation (Somerville *et al.*, 1974). The underestimate of the strength of the Hadley cells may be due to the omission from the model of any vertical mixing of momentum by moist convection (Stone *et al.*, 1974; Schneider and Lindzen, 1976). The strength of the Ferrel cells is closely related to the strength of the eddy fluxes (Kuo, 1956). Consequently the weakness of the simulated Ferrel cells may be attributed to the underestimate of the eddy flux of momentum in the simulations (see Fig. 3.7).

Figs. 3.5 and 3.6 show the zonal mean temperature and specific humidity fields, respectively, from the July simulation, together with the observed fields, based on Oort and Rasmusson's (1971) data. The simulated temperature field is generally in good agreement with the observations in the troposphere. For example, the tropospheric static stabilities are within 0.5 K km⁻¹ of the observed static stabilities. The most notable discrepancies in the temperature are in the stratosphere where the model's vertical resolution is poor. Here the simulated equatorial temperatures are about 10 K too warm. The simulated specific humidity field is on the whole realistic. Near the surface in tropical regions, the simulated humidity falls off more rapidly with height than in the observations, because the simulated equatorward branch of the Hadley cell and its associated moisture transport are too strongly peaked near the ground (see Figs. 3.4 and 3.12).
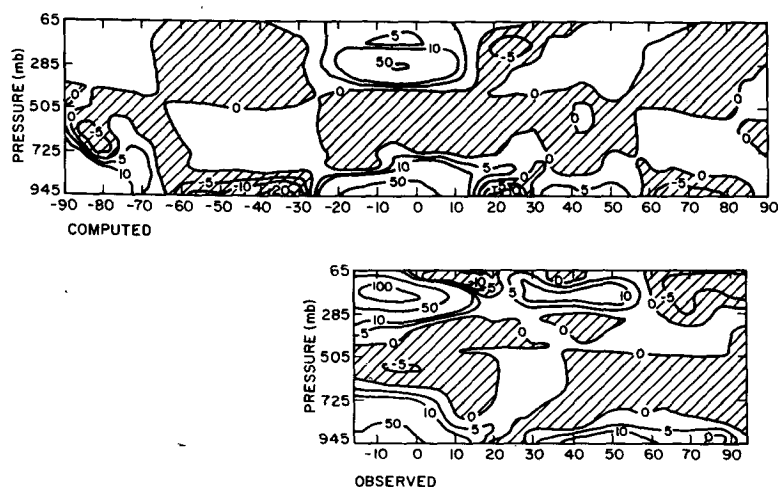


FIG. 3.10. As in Fig. 3.7 except for northward transport of sensible heat by the mean
meridional circulations. Units: °C m s⁻¹.
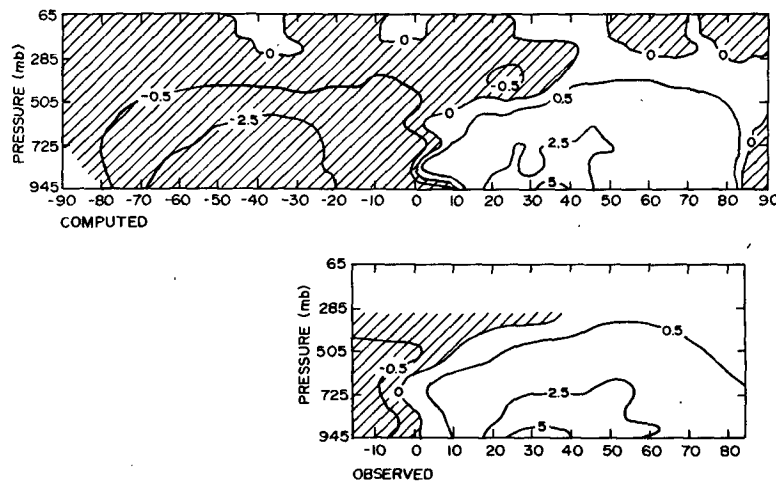
FIG. 3.11. As in Fig. 3.7 except for northward transport of water vapor by eddies.
Units: g kg$^{-1}$ m s$^{-1}$.

## c. Meridional transports

Figs. 3.7–3.12 show the simulated and observed zonal mean fields of the meridional transports of westerly momentum, sensible heat and water vapor by eddies and by the mean meridional circulations. The observed fields are based on Oort and Rasmusson's data (1971). In calculating the transports we have followed Oort and Rasmusson's (1971) definitions of the transports. Qualitatively, the simulated meridional transports are realistic. For example, the transports in low latitudes are dominated by the Southern Hemisphere Hadley cell (Figs. 3.8, 3.10 and 3.12) while the transports in mid and high latitudes are dominated by the eddies (Figs. 3.7, 3.9 and 3.11); the eddy momentum transport tends to concentrate the mid-latitude jets (Fig. 3.7); the poleward transport of sensible heat by the eddies shows the characteristic double maximum in mid-latitudes, one near the surface and one near the tropo-

pause (Fig. 3.9); and the poleward transport of water vapor by the eddies is concentrated near the surface in mid-latitudes (Fig. 3.11). The simulated locations of the maxima in the different components of the meridional transports are also in very good agreement with the observed locations.

However, the strength of the transports is generally underestimated in the July simulation, just as it was in the January simulation (Somerville et al., 1974). The previously described underestimate of the strength of the Hadley and Ferrel cells causes the transports of momentum and sensible heat by the mean meridional circulations to be about one-half as large as the observed transports in the poleward branch of the Southern Hemisphere Hadley cell, and much smaller than the observed transports in mid-latitudes (Figs. 3.8 and 3.10). The maximum in the eddy transport of momentum near the tropopause in mid-latitude is
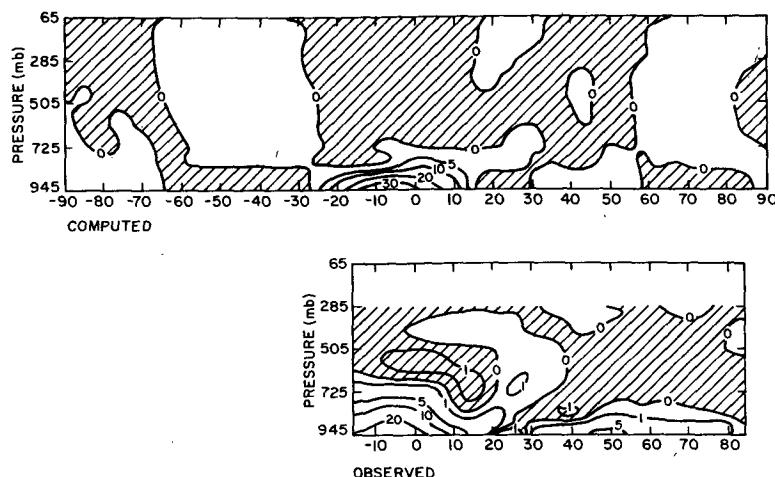


FIG. 3.12. As in Fig. 3.7 except for the northward transport of water vapor by the mean meridional circulations. Units: g kg$^{-1}$ m s$^{-1}$.

about one-third as strong in the simulation as in the observations (Fig. 3.7). This deficiency is to be expected in view of the model's underestimate of the strength of eddies in general (see Section 4a). Underestimates of the eddy momentum transport appear to be common in general circulation models with comparable horizontal resolution (Manabe et al., 1970; Kasahara et al., 1973). On the other hand, the simulated maximum in the eddy transport of sensible heat is much more realistic (Fig. 3.9). The maximum water vapor transport by the equatorward branch of the Southern Hemisphere Hadley cell is overestimated in the simulation (Fig. 3.12), but this transport is also too sharply peaked near the ground, so the total transport in the simulation is close to the observed transport.

### d. Kinetic energy spectrum

Fig. 3.13 shows the eddy kinetic energy spectrum for the Northern Hemisphere troposphere (levels 2–9) in the July simulation. Saltzman's (1970) conventions were used in calculating the spectrum. The eddy kinetic energy peaks at low wavenumbers, but does not fall off sharply with wavenumber until wavenumbers $> 9$ are reached. In January the sharp fall-off in the simulated spectrum occurred after wavenumber 5 (Somerville et al., 1974). In the wavenumber range 8–15 the computed spectrum has an approximate $-2.4$ power dependence on wavenumber in July, and an approximate $-2.5$ power dependence in January. These results may be compared with the $-3$ power dependence of geostrophic or two-dimensional turbulence. At all wavenumbers, the kinetic energy in July is less than in January, with the difference being largest at wavenumbers 2–5.
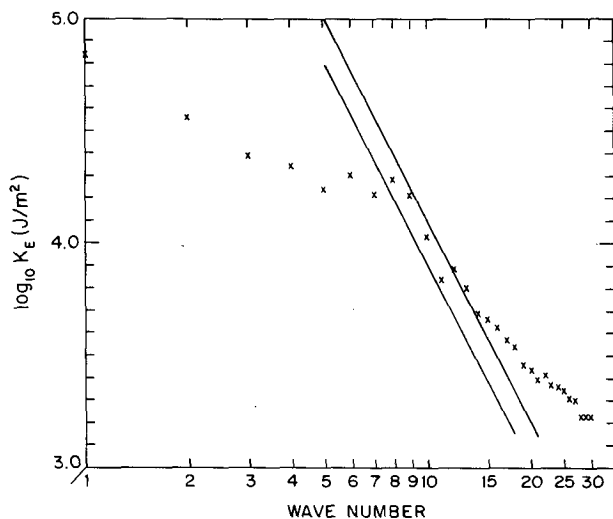


FIG. 3.13. Computed July mean eddy kinetic energy $(K_E)$ vs zonal wavenumber. The slanted lines show a $-3.0$ slope.

### e. Diabatic heating

Figs. 3.14a and 3.14b show the zonal mean radiative heating rates due to solar and terrestrial radiation, respectively, calculated from the July simulation. The distributions are in good qualitative agreement with independent calculations (e.g., Dopplick, 1972). Quantitative checks of the simulated atmospheric heating rates are not yet possible since they are very sensitive to the vertical distribution of cloud cover used in the calculations (Haurwitz and Kuhn, 1974), and the actual vertical distribution is not well known. The seasonal changes in the simulated radiative heating rates agree with one's expectations: reflecting the January heating rates about the equator would give a good approximation to the July heating rates.

Figs. 3.14c and 3.14d show the zonal mean heating rates in the July simulation due to large-scale supersaturation and to parameterized subgrid-scale moist convection, respectively. The latter process dominates in the tropics, and the former in middle and high latitudes. Again the July heating rates represent approximately a reflection of the January heating rates about the equator. Other diabatic process in the model, i.e., subgrid-scale diffusion and dry convection, have negligible atmospheric heating rates compared to those illustrated in Fig. 3.14.

## 4. Seasonal differences

In this section we present results from the July simulation described in the preceding section, together with results from the January simulation and from observations, in order to ascertain the model's ability to simulate seasonal differences. The January and July simulations described here differ only in the choice of initial conditions and boundary conditions. The January simulation results differ slightly from those presented by Somerville et al. (1974) because they use the modified formula for the eddy diffusion coefficients in the lowest layer referred to in Section 2, and because all of the present calculations are based on a sampling interval of 4 h instead of 12. Experiments with different sampling intervals showed that an interval of 4 h was small enough to reduce errors in all the computed fields compared to a true time average to no more than a few percent, with the exception of the rainfall maps (see Section 4e). In addition, the latitude-height distributions of eddy transports of momentum, sensible heat and water vapor published in Somerville et al. (1974) were inaccurate, because of a programming error in the diagnostic code. The difference between the published transports and the corrected transports is 10–20%.

### a. Energy cycle

One convenient measure of the overall performance of a general circulation model is the accuracy with which it simulates the atmosphere's energy cycle. The
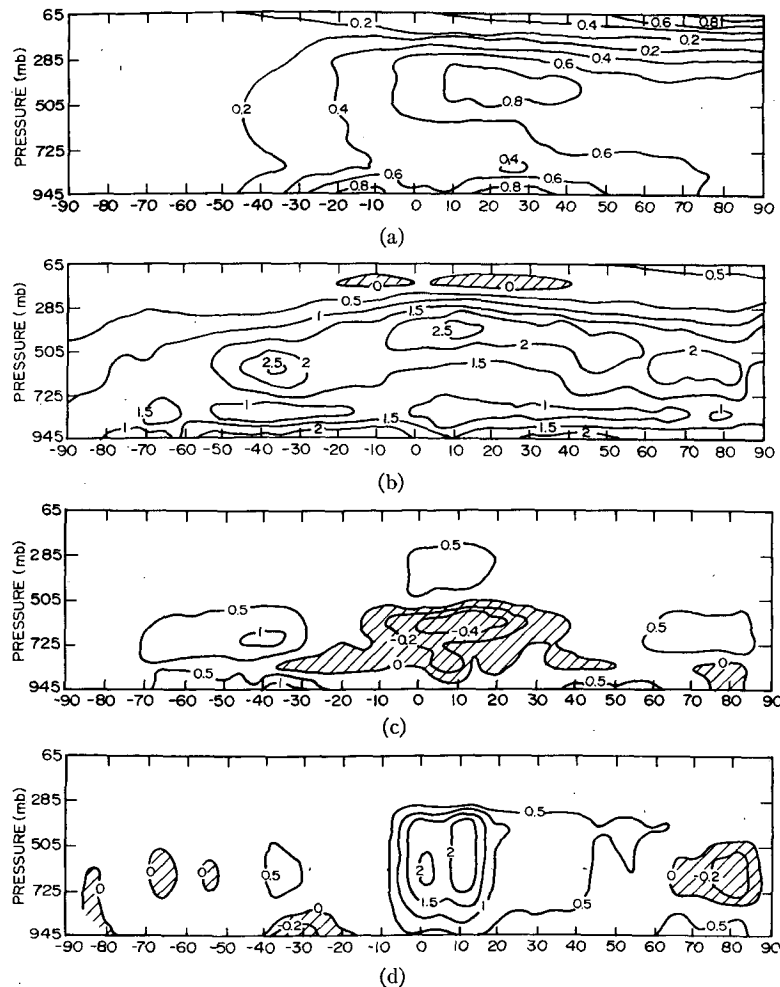
FIG. 3.14. Computed July zonal mean fields of diabatic heating rates: (a) heating
due to solar radiation, (b) cooling due to terrestrial radiation. Negative regions
(regions of heating) are shaded. (c) Heating due to large scale condensation and
evaporation. Negative regions (regions of net evaporation) are shaded. (d) Heating
due to parameterized subgrid-scale moist convection. Negative regions are shaded.
Units: °C day$^{-1}$.

simulated energy cycles in the Northern Hemisphere troposphere (levels 2 to 9) for January and July are shown in Fig. 4.1. The corresponding observed energy cycles estimated by Oort and Peixoto (1974) are shown in parentheses in Fig. 4.1. The new symbols in the figures are defined as follows:

$G(X)$ —generation of $X$

$D(X)$ —dissipation of $X$

$C(X,Y)$—conversion of $X$ to $Y$

The model's energetics were computed for the mixed space-time domain using the same formulas as Oort and Peixoto (1974) with the exception of $C(P_M, K_M)$. Oort and Peixoto calculated this conversion from

$$C(P_M, K_M) = - \int [\bar{v}]g \frac{\partial [\bar{z}]}{a \partial \phi} dm,$$

whereas the model-generated value was calculated from the more common definition (Oort, 1964; Saltzmann, 1970)

$$C(P_M, K_M) = - \int [\bar{\omega}]''[\bar{\alpha}]'' dm.$$

[Oort and Peixoto's (1974) notation is used in these expressions.] For the global domain these two formulations are identical, but for the hemispheric domain they differ considerably because the flux of potential energy across the equator is significant (see Fig. 4.11). The previously published calculations for the simulated energy cycle in January (Somerville et al., 1974) used Oort's (1964) approximate formulas, which neglect variations of the static stability. Oort and Peixoto's (1974) formulas do not neglect these variations and give substantially different results for $P_M$ and $P_E$. Consequently, the energy box diagrams presented here
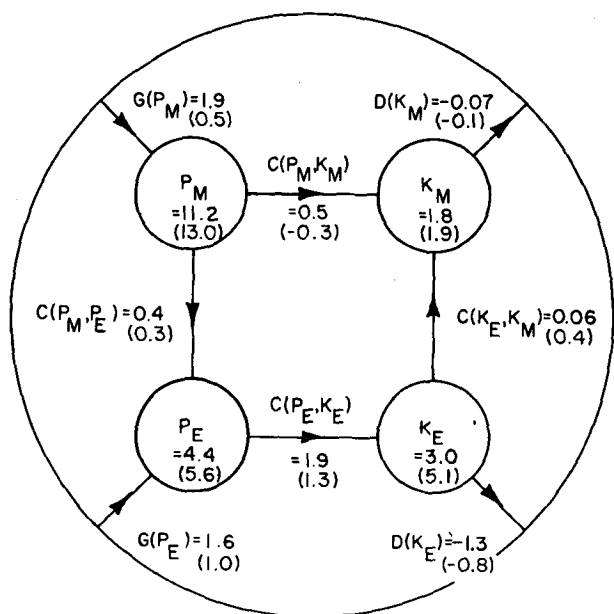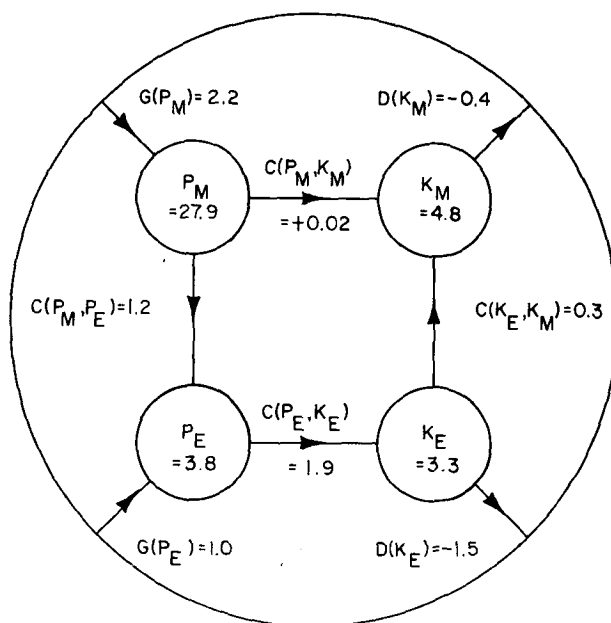
JANUARY
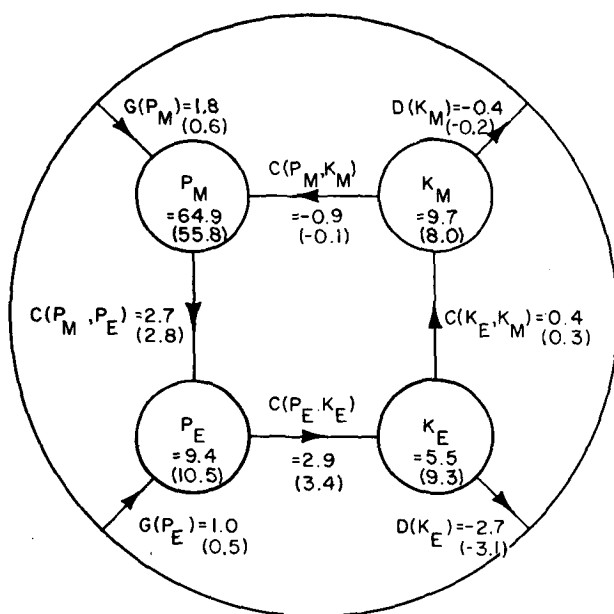


JULY



FIG. 4.1. Simulated energy cycle for the Northern Hemisphere troposphere. (a) January, (b) July. Units: energy, $10^5$ J m$^{-2}$; conversions, W m$^{-2}$. Observed values from Oort and Peixoto (1974) are given in parentheses.

use the exact formulas, and the diagram for January in Fig. 4.1 differs from that presented by Somerville *et al.* (1974).

The simulated Northern Hemisphere energy cycle and its seasonal differences agree quite well with the observations. The most notable discrepancy in the

simulations is the underestimate of $K_E$. This is a common feature of general circulation models, apparently caused largely by inadequate horizontal resolution (Manabe *et al.*, 1970; Wellck *et al.*, 1971). However, even for $K_E$ the simulated seasonal difference is accurate, i.e., the July value is 55% of the January value in both the simulations and the observations. The January values of $P_M$ and $K_M$ in the simulations are
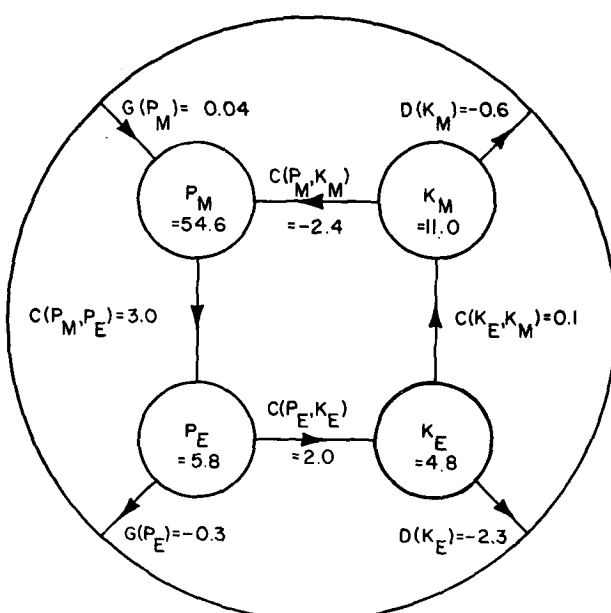
JANUARY



JULY



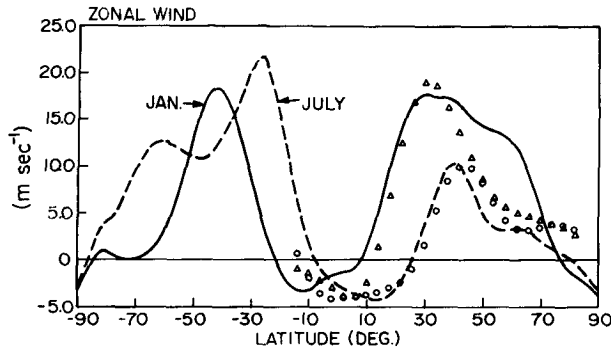FIG. 4.2. As in Fig. 4.1 except for the Southern Hemisphere.

FIG. 4.3. Latitudinal distributions of vertically averaged tropospheric zonal wind from the simulations for January (solid line) and July (dashed line), together with the observed values for January (triangles) and July (circles). The observed field is based on data from Oort and Rasmusson (1971).

about 20% higher than in the observations, because the meridional temperature gradient in the simulated January is too large (see Fig. 4.9). Because of this larger gradient, the meridional deviation from the area mean temperature on isobaric surfaces is increased, thus increasing $P_M$, and the mean zonal thermal wind is increased, thus increasing $K_M$. It is not clear whether the discrepancy between the simulated and observed values of $G(P_M)$ is significant. The "observed" values were in fact calculated as residuals, and different methods of estimating $G(P_M)$ give substantially different values (Oort and Peixoto, 1974).

The simulated energy cycle for the Southern Hemisphere troposphere (levels 2–9) is shown in Fig. 4.2 for January and July. The energy cycle is qualitatively similar to that for the Northern Hemisphere. However, the seasonal differences in the Southern Hemisphere are significantly smaller than in the Northern Hemisphere probably because of the moderating influence of the greater ocean area in the Southern Hemisphere.

## b. Momentum balance

Fig. 4.3 shows the latitudinal distribution of vertically averaged mean zonal wind for the model atmosphere for January and July, together with the observed values based on data from Oort and Rasmusson (1971). In all the subsequent figures in this section with the same format as Fig. 4.3, the solid curves refer to the simulated January atmosphere, the dashed curves to the simulated July atmosphere, the triangles to the observed January atmosphere, and the circles to the observed July atmosphere. The vertical averages are all computed for the troposphere, i.e., for the model the data are averaged over layers 2 to 9, corresponding approximately to pressures from 120 mb to the surface, and for the observations (Oort and Rasmusson, 1971) the data are averaged over pressures from 125 to 1012.5 mb.

Fig. 4.3 shows that the seasonal variation in the Northern Hemisphere jet is simulated accurately by the model. In particular, the jet is displaced 10° northward in July, and is only half as strong as in January. As reported previously (Somerville, 1974), the model-calculated Northern Hemisphere jet in January is too broad, because the model-calculated meridional temperature gradient in northern high latitudes is too large (see Fig. 4.9). The width of the Northern Hemisphere jet in July is simulated much more accurately. The seasonal variation in the strength of the jet in the Southern Hemisphere is much less pronounced than in the Northern Hemisphere, in agreement with observations (van Loon, 1972).

Fig. 4.4 shows the meridional streamfunction from the simulations and the observations for January [not given in Somerville et al., (1974)]. This may be compared with the July streamfunction shown in Fig. 3.4. The model's underestimate of the strength of the meridional calculation is again apparent, but the underestimate in January and July is consistent so that the
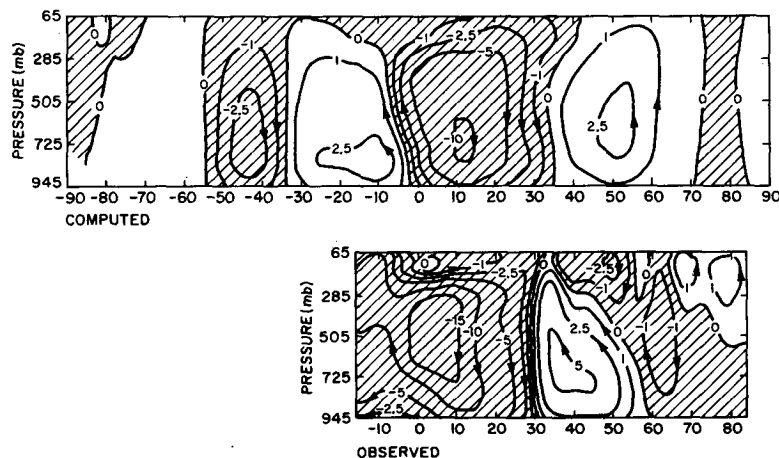


FIG. 4.4. Computed and observed January streamlines of the monthly mean meridional circulation. The observed field is based on data from Oort and Rasmusson (1971). Units are $10^{10}$ kg s$^{-1}$. Negative regions are shaded.
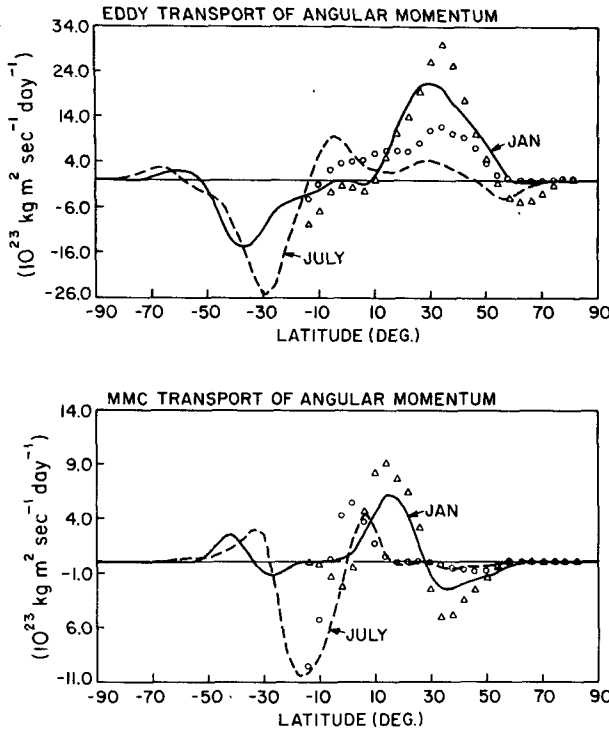
EDDY TRANSPORT OF ANGULAR MOMENTUM



MMC TRANSPORT OF ANGULAR MOMENTUM



FIG. 4.5. As in Fig. 4.3 except for northward transport of angular momentum by (a) eddies, and (b) mean meridional circulations.
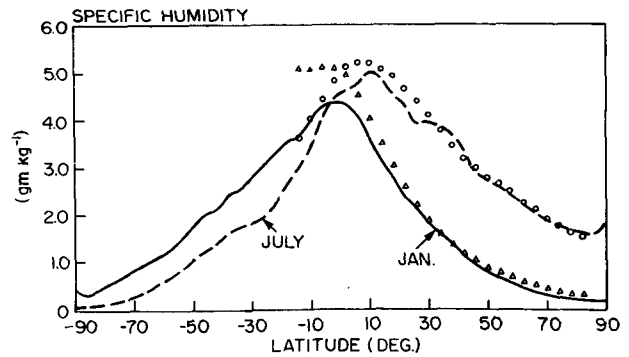
SPECIFIC HUMIDITY



FIG. 4.6. As in Fig. 4.3 except for specific humidity.

Hemisphere. In particular, the strength of the Ferrel cell in the Southern Hemisphere shows virtually no difference in July compared to January. The model's underestimate of the circulation in the Hadley cells is less in the Southern Hemisphere than in the Northern Hemisphere.

Fig. 4.5 shows the latitudinal distribution of the northward transport in the troposphere of relative angular momentum by the large-scale eddies (transient plus stationary) and by the mean meridional circulations for both January and July, as simulated by the model, together with the observed transports based on data from Oort and Rasmusson (1971). The results are what one would expect from the already quoted results for eddy kinetic energy and the mean meridional streamfunction. The eddy transports and mean transports are underestimated in the simulations, but their seasonal variations are simulated reasonably well. In the summer the mean transports virtually disappear and the eddy transports are reduced, by a substantial amount in the Northern Hemisphere and by a lesser amount in the Southern Hemisphere.

seasonal differences are simulated accurately. In both the simulations and the observations, the Northern Hemisphere Hadley cell all but disappears in July and the Northern Hemisphere Ferrel cell is only about one-third as strong in July as in January. The seasonal behavior in the Southern Hemisphere in the simulations contrasts strongly with the behavior in the Northern
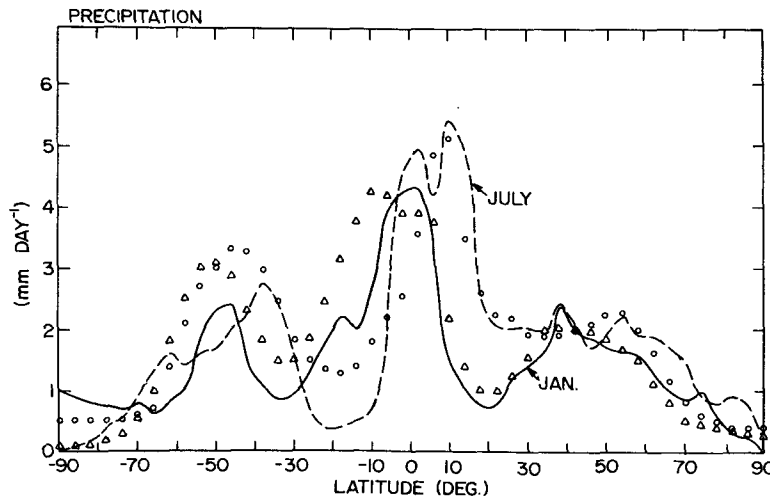
PRECIPITATION



FIG. 4.7. As in Fig. 4.3 except for distribution of zonally averaged precipitation. The observed values are seasonal means from Möller (1951) as analyzed by Schutz and Gates (1972a,b).
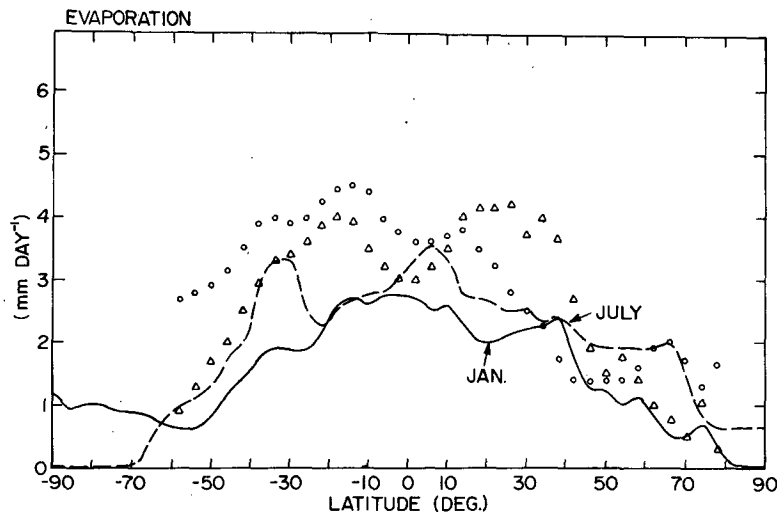
EVAPORATION

FIG. 4.8. As in Fig. 4.3 except for evaporation. The observed values are from Budyko (1963), as analyzed by Schutz and Gates (1971, 1972b).

## c. Hydrological cycle

Fig. 4.6 shows the tropospheric mean specific humidity as a function of latitude for January and July, both from the simulations and from the observations (Oort and Rasmusson, 1971). The model's underestimate of the strength of the winter Hadley cell leads to an underestimate of the moisture transport by the equatorward branch of the Northern Hemisphere Hadley cell in January (see Fig. 4.12), and this results in an underestimate of the humidity near the equator in the January simulation, as is apparent in Fig. 4.6. However, Fig. 4.6 shows that on the whole the simulated seasonal differences in the humidity agree quite well with the observations. This good agreement is not surprising when one considers that the specific humidity is strongly controlled by the temperature through the Clausius-Clapeyron relation and that the sea-surface temperatures in the simulations are prescribed to have the observed January and July values. The simulated seasonal differences in the humidity of the Southern Hemisphere are again much smaller than in the Northern Hemisphere because of the greater moderating effect of the southern oceans.

Figs. 4.7 and 4.8 show the zonal mean precipitation and evaporation rates, respectively, for January and July, from the simulations and the observations. The observed values in both figures are taken from Möller (1951) and Budyko (1963), respectively, as analyzed by Shutz and Gates (1971, 1972a, b). The observed precipitation rates are actually seasonal rates, i.e., means for December-January-February and June-July-August, rather than for January and July. The simulated seasonal differences in the precipitation rates are in good agreement with the observations. In particular, the differences are small, except in the subtropics where the rainfall is substantially increased in summer.

The simulated evaporation rates shown in Fig. 4.8 are systematically lower than the observed (actually inferred) rates in low latitudes. Most of the evaporation comes from the ocean surface, which is prescribed to have the correct climatological temperature for each month. However, the simulated atmospheric specific humidities near the surface are high (see Fig. 3.6) and this probably accounts for the underestimate of the evaporation rates.

## d. Heat balance

Fig. 4.9 shows the mean tropospheric temperature for January and July as a function of latitude, from both the simulations and the observations (Oort and Rasmusson, 1971). In low and mid latitudes, the seasonal temperature variation has been simulated accurately. However, there is a notable discrepancy in north polar regions. These regions are as much as 10 K too cold in the January simulation, although they are simulated much more accurately in July. It is the resulting overestimate of the meridional temperature gradient in the simulated January which causes the
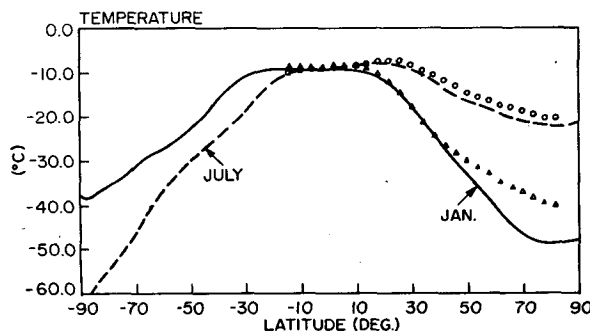
TEMPERATURE

FIG. 4.9. As in Fig. 4.3 except for temperature.
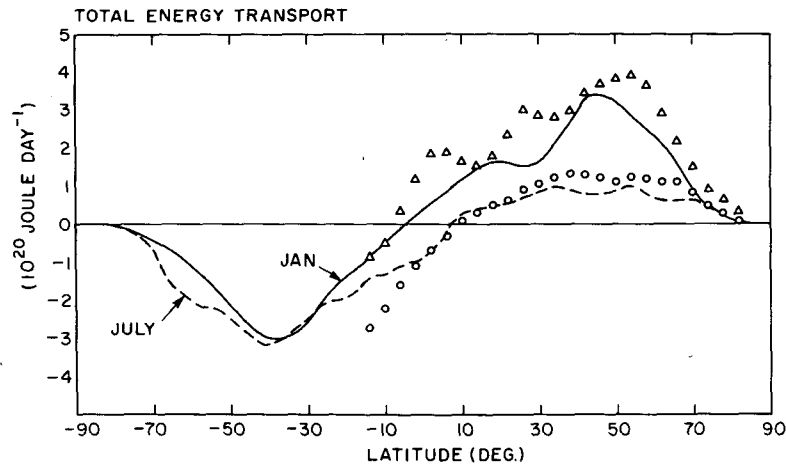
TOTAL ENERGY TRANSPORT



FIG. 4.10. As in Fig. 4.3 except for total energy transport across a latitudinal circle.

broadness of the jet and the overestimate of $K_M$ and $P_M$ in the Northern Hemisphere in January. In addition, the simulated Northern Hemisphere temperatures in July are systematically 1–2 K too cold.

Other GCM's with similar horizontal resolution show comparable discrepancies in north polar regions in January (Holloway and Manabe, 1971; Kasahara et al., 1973; Newson, 1974). In these latitudes the amount of solar heating is negligible in January, and there are very few ocean grid points (which act as heat reservoirs in the model). Consequently, the temperatures are determined essentially by a balance between the import of heat by atmospheric motions from low latitudes and the export of heat by longwave radiation to space. The lower temperatures in the simulations thus imply that the dynamical heating and longwave cooling are both reduced compared to the atmospheric situation. In fact the model-simulated longwave radiation to space in the arctic regions in January is about 20% smaller than the amount measured from satellites (Vonder Haar and

Suomi, 1971). This reduction is what one would expect for lower temperatures.

On the other hand, the lower temperatures imply larger meridional temperature gradients, as illustrated in Fig. 4.9. One would expect these increased gradients to be accompanied by an increased dynamical flux into arctic regions in January. Actually, the dynamical flux in the January simulation is reduced, as shown in Fig. 4.10. This figure shows the meridional tropospheric flux across a latitude circle of total energy (potential energy plus latent heat plus sensible heat plus kinetic energy) by all atmospheric motions as a function of latitude, calculated both from the simulations and from the observations (Oort and Rasmusson, 1971). At 58°N in January the simulated transport is about 30% less than the observed transport, and this reduction implies a decrease in the mean dynamical heating rate in higher latitudes of about 0.3°K per day. This reduction in the dynamical flux is the apparent cause of the low arctic temperatures in January. Discrepancies
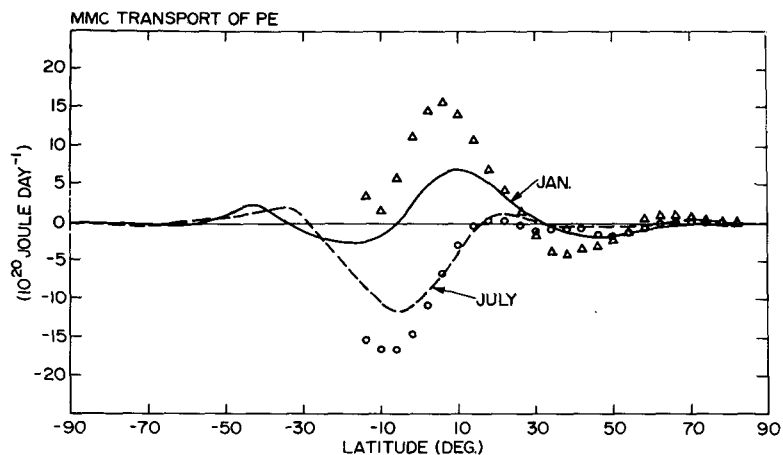
MMC TRANSPORT OF PE



FIG. 4.11. As in Fig. 4.10 except for transport of potential energy by the mean meridional circulations.
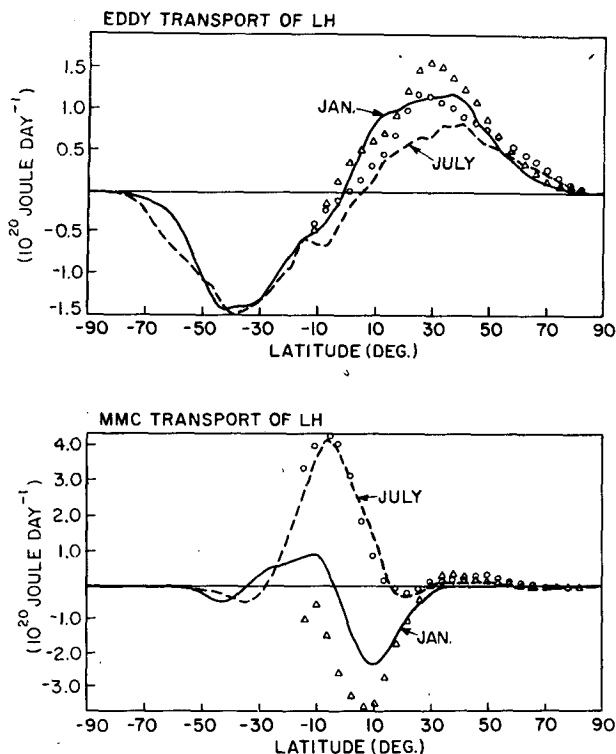
EDDY TRANSPORT OF LH



MMC TRANSPORT OF LH



FIG. 4.12. As in Fig. 4.10 except for transport of latent heat by (a) eddies and (b) mean meridional circulation.

in the total meridional flux at lower latitudes have a much smaller impact on mean temperatures because they are spread over much larger areas and because of the stabilizing effect of specifying sea surface temperatures. Similar deficiencies in the dynamical heating rate in north polar regions are apparent in January simulations by other GCM's with comparable resolution (Holloway and Manabe, 1971; Kasahara et al., 1973). By contrast, Fig. 4.10 shows that the simulation of the meridional energy flux in July is much more realistic.

Figs. 4.11, 4.12 and 4.13 show the individual components of the meridional energy flux which make significant contributions to the total flux, i.e., the flux of potential energy by the mean meridional circulations (Fig. 4.11), and the fluxes of latent heat (Fig. 4.12) and sensible heat (Fig. 4.13) by the large-scale eddies and by the mean meridional circulation. Once again these figures show the mean tropospheric fluxes as a function of latitude for both January and July, calculated from both the simulations and the observations (Oort and Rasmusson, 1971). The seasonal variations in these fluxes are in good qualitative agreement with the observations. For example, the seasonal reversal in sign of the cross-equatorward transports by the mean meridional circulation and the sharp decrease in the transports by the Hadley cells in summer (Figs. 4.11, 4.12b, 4.13b), and the sharp decrease in the eddy transport of sensible heat in the Northern Hemisphere in summer (Fig. 4.13a) are reproduced by the simula-

tions. However, the deficiencies noted previously— namely the underestimates of the strength of the Hadley cells and of the activity of the large scale eddies—again cause most of the individual components of the meridional flux to be underestimated. The seasonal differences in the Southern Hemisphere are again much less than in the Northern Hemisphere. The seasonal differences in the eddy latent heat flux (Fig. 4.12a) are much less than the seasonal differences in the eddy sensible heat flux (Fig. 4.13a), because seasonal changes in eddy activity tend to be compensated by seasonal changes in specific humidity (cf. Figs. 4.1 and 4.6).

Figs. 4.11–4.13 show that the deficiency in the dynamical heating of north polar regions in January is primarily due to the underestimate of the eddy flux of sensible heat. This flux can be separated into the contributions by stationary eddies and by transient eddies, and it then becomes apparent that the main deficiency is in the stationary eddy flux of sensible heat in mid-latitudes. Fig. 4.14 shows this flux calculated for the troposphere as a function of latitude from the simulations and also from observations (Oort and Rasmusson, 1971). Since the stationary eddies virtually disappear in summer, errors in simulating the associated flux only affect the simulation of north polar temperatures in January. Spectral analysis of the GISS model's energetics (Tenenbaum, 1976) shows that the deficiency in the meridional heat transport is associated primarily with zonal wavenumber 3. These results taken together

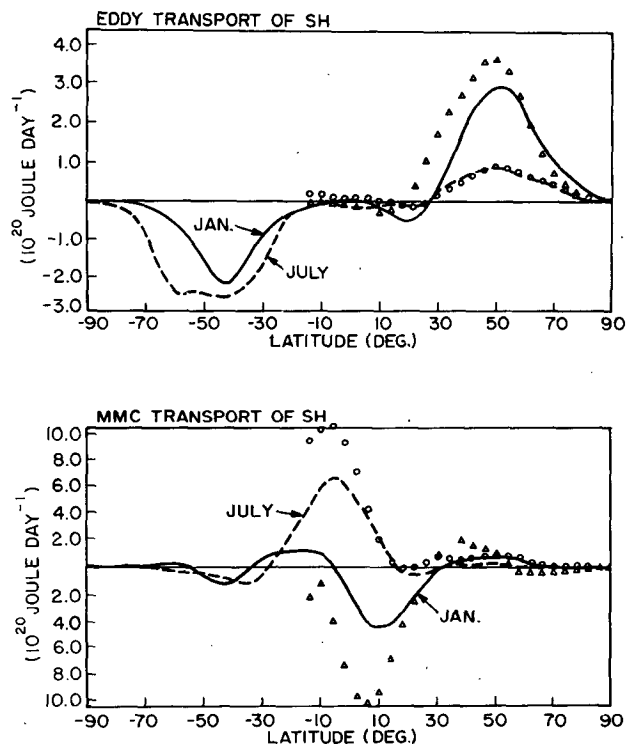EDDY TRANSPORT OF SH



MMC TRANSPORT OF SH



FIG. 4.13. As in Fig. 4.10 except for transport of sensible heat by (a) eddies and (b) mean meridional circulations.
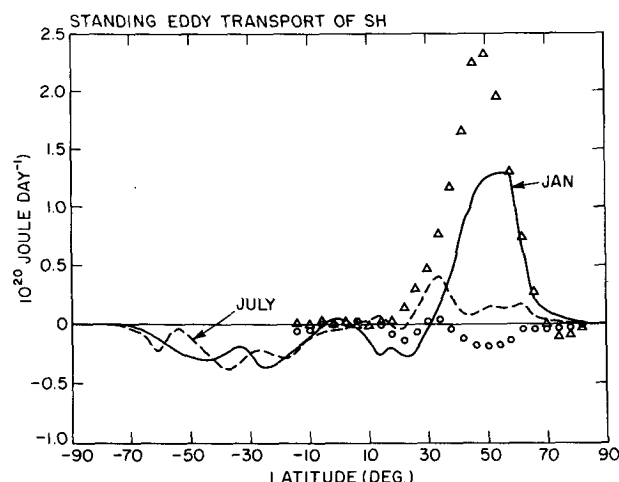
FIG. 4.14. As in Fig. 4.10 except for transport of sensible heat by stationary eddies.

suggest that the cold arctic temperatures simulated in January are caused by an inadequate simulation of the Aleutian and Icelandic lows (cf. Figs. 4.16 to 4.19).

The discrepancy in the July temperatures in the Northern Hemisphere is systematic (see Fig. 4.9) and cannot be explained by deficiencies in the dynamical heating rates, which in July are not systematically high or low (see Fig. 4.10). Rather the discrepancy must be attributed to deficiencies in the simulation of the radiative heating. In particular, the lower temperatures in the July simulation imply that the simulated absorption of shortwave radiation and emission of longwave radiation are too low.

The deficit in the shortwave absorption is revealed in the calculated value of the global albedo. In the July simulation this is 0.346, whereas the mean value measured by satellites for the months of June, July and August is 0.26 (Vonder Haar and Suomi, 1971). This discrepancy is more than ample to account for the 1–2 K discrepancies shown in Fig. 4.9. The discrepancy would be even greater if it were not for the stabilizing effect of prescribing sea surface temperatures. No comparable discrepancy in the albedo appeared in the January simulation. The simulated mean global albedo for January was 0.325, which may be compared to the observed value for the months of December, January and February of 0.31 (Vonder Haar and Suomi, 1971). It is noteworthy that the simulated seasonal variation in the global mean albedo has the wrong sign.

The main contributor to the global mean albedo is cloud albedo. Table 4.1 shows the percentage cloud cover for each hemisphere and each season in the simulations, broken down by cloud type. In general the convective clouds are more numerous in summer, while the supersaturation clouds are less numerous. Thus, changes in the two cloud types tend to compensate each other. The total cloud cover shows opposite tendencies in the different hemispheres, increasing in

TABLE 4.1. Simulated percentage cloud covers.

| Cloud type | Northern Hemisphere January | July | Southern Hemisphere January | July |
|---|---|---|---|---|
| Low-level convective clouds | 7 | 8 | 6 | 9 |
| Mid-level convective clouds | 2 | 3 | 3 | 3 |
| Penetrating convective clouds | 5 | 12 | 7 | 4 |
| All convective clouds | 12 | 21 | 14 | 13 |
| Supersaturation clouds | 45 | 44 | 40 | 47 |
| All clouds | 49 | 52 | 45 | 50 |

summer in the Northern Hemisphere, but increasing in winter in the Southern Hemisphere. The simulated total cloud cover in the Northern Hemisphere is in excellent agreement with the observed values of 0.48 in January and 0.52 in July (Sasamori et al., 1972). Also the distribution of convective cloud types is realistic, in particular the dominance of low-level and deep-penetrating convection (Ogura and Cho, 1973). However, the seasonal tendency in the total cloud cover in the Southern Hemisphere is opposite to that reported by Sasamori et al. (1972).

Fig. 4.15 shows the latitudinal variations of mean cloud cover due to supersaturation clouds and convective clouds. In this figure the cloud covers generated by the simulations are compared with observed values based on the analysis by Rodgers (1967) for the Northern Hemisphere and by Sasamori et al. (1972) for the Southern Hemisphere. In calculating the observed cloud covers from the cloud covers for individual cloud types, we assumed that cloud types occurring at different levels had a random overlap. These figures
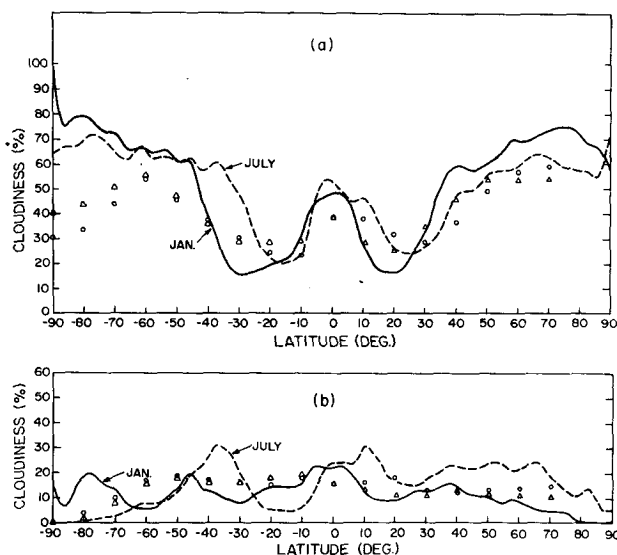


FIG. 4.15. Latitudinal distribution of cloud cover. The observed values are based on data from Rodgers (1967) for the Northern Hemisphere and from Sasamori et al. (1972) for the Southern Hemisphere. (a) supersaturation clouds, (b) convective clouds.
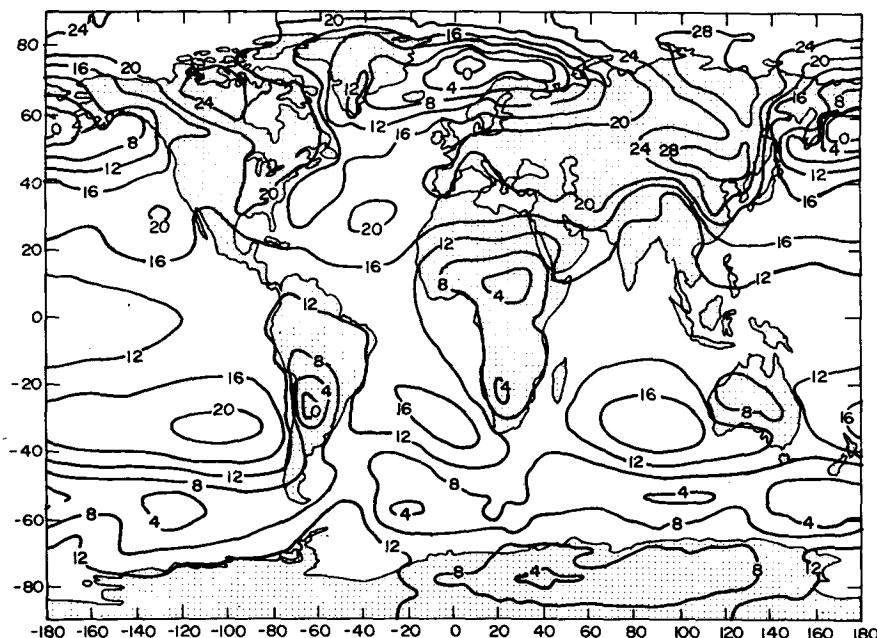
FIG. 4.16. Contours of sea level pressure minus 1000 mb in the model-simulated January. The pressures have been smoothed with a weighted five-point formula giving a weight of $\frac{1}{8}$ to the four adjacent points.

show that the simulated seasonal differences in the Northern Hemisphere are realistic as far as the super-saturation clouds are concerned, but are much too large as far as the convective clouds are concerned. This increase in the convective cloud cover in the Northern Hemisphere summer is mainly attributable to the increase in penetrating convective clouds (see Table 4.1). Since these clouds have albedos of 0.81 (see Table 2.1) the discrepancy in the deep convective clouds could account for much of the discrepancy in the albedo in the July simulation. The poor simulation of the deep, penetrating convective cloud cover can be attributed to inadequacies in the parameterization scheme for moist convection as discussed by Stone et al. (1975). It is interesting to note that this discrepancy was not accompanied by a similar discrepancy in the precipitation in the Northern Hemisphere (see Fig. 4.7).

In the Southern Hemisphere the convective cloud cover in the simulations shows strong local variations, but in a mean sense is in reasonable agreement with the observations. The simulated supersaturation cloud cover in the Southern Hemisphere is systematically larger than the cloud covers reported by Sasamori et al. (1972), but satellite observations (Clapp, 1964) also give substantially larger estimates of cloud cover in the Southern Hemisphere. The marked increase in the supersaturation cloud cover in the subtropics of the Southern Hemisphere in July accounts for the increase in the total cloud cover in the Southern Hemisphere in July (see Table 4.1) and for the apparent discrepancy with the observed seasonal change in the Southern Hemisphere (Sasamori et al., 1972).

### e. Horizontal structure of the simulated climates

Figs. 4.16 and 4.17 show the simulated sea-level pressures for January and July, respectively. Fig. 4.16 differs significantly from the sea-level pressures given by Somerville et al. (1974) because of the change in the formula for the eddy diffusion coefficient in the lowest layer described in Section 2. This change led to much more realistic sea-level pressures. The semi-permanent pressure systems and their seasonal differences are generally reproduced accurately. For example, the Icelandic low and Siberian high are present in January but not in July; the low in the Gulf of Alaska in January is replaced by a high in July; and the Himalayan low and Australian high are present in July but not in January. The primary defect in the simulations is the sea-level pressures over mountainous regions. For example, the low over the Andes in January and the high over the Antarctic in July are unrealistic, and the low pressures over the Himalayas in July are too extreme. Also the low pressures surrounding Antarctica are underestimated. The "sea level" pressures shown for mountainous regions are, of course, extrapolated pressures rather than true pressures. Similar discrepancies in sea level pressures over mountainous regions occur in other GCM's (Manabe and Holloway, 1975).

Figs. 4.18 and 4.19 show the simulated 500 mb geopotential height surfaces for January and July, respectively. Again the seasonal differences in the major features are realistic. For example, the mid-latitude gradients are much weaker in summer, and the ridge
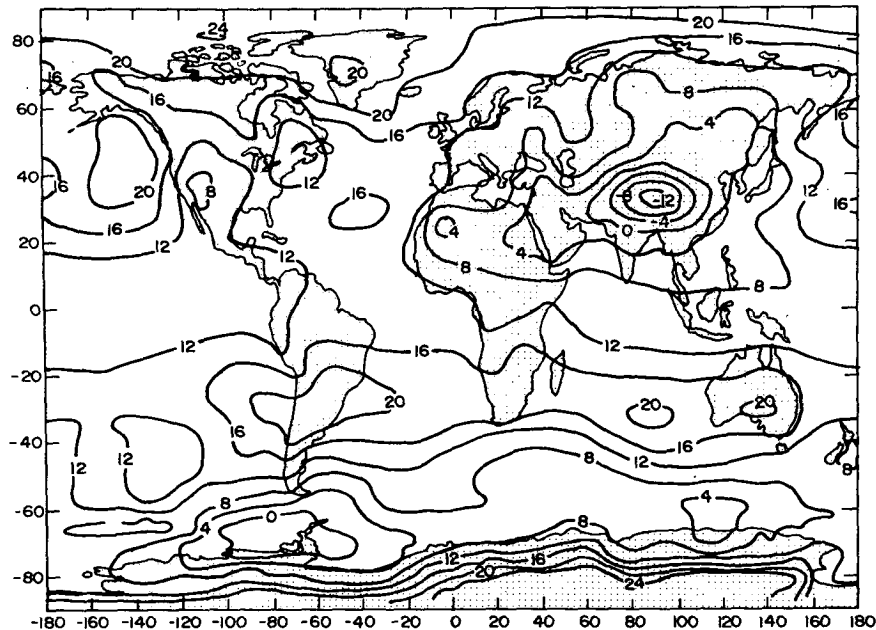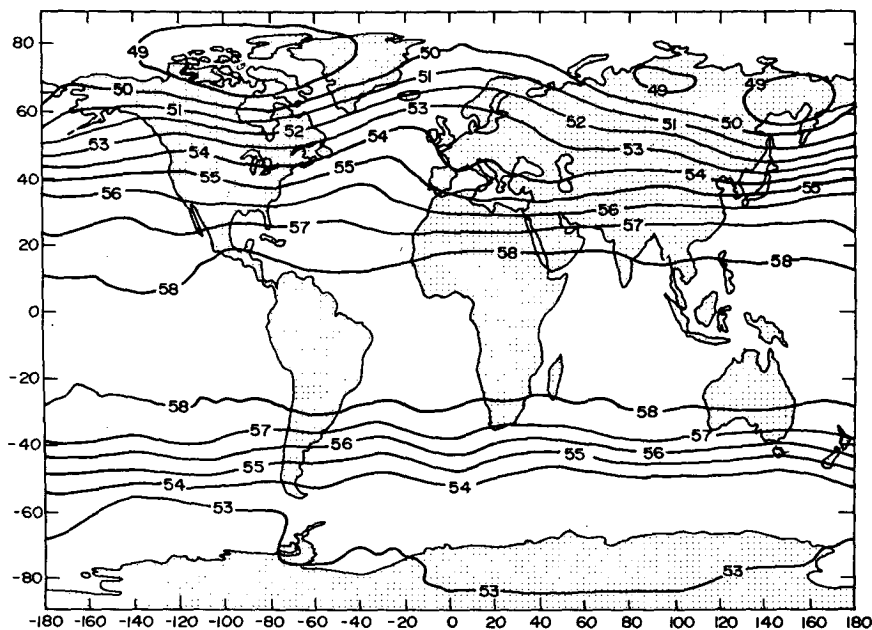
FIG. 4.17. As in Fig. 4.16 except for July.

over the Eastern Atlantic is much weaker in July than in January.

Fig. 4.20 and 4.21 show maps of the model-generated surface winds for January and July, respectively. The surface winds shown here were calculated by linearly extrapolating the velocities in layers 8 and 9 to the earth's surface. The main features and their seasonal differences are simulated realistically. For example, the trade winds and the intertropical convergence zone (ITCZ), their northward shift in July, and the seasonal reversal of the monsoonal circulation over India are all readily apparent. In January, however, the low-level winds in the Bay of Bengal and southeast Asia are much too weak and in the wrong direction (Riehl, 1954). This defect is probably caused by the fact that the simulated Siberian high in January is weaker and farther east than in reality (see Fig. 4.16). Also, there is a tendency for the simulated ITCZ in the Indian



FIG. 4.18. Contours of 500 mb geopotential height in $10^2$ m for the model-simulated January.
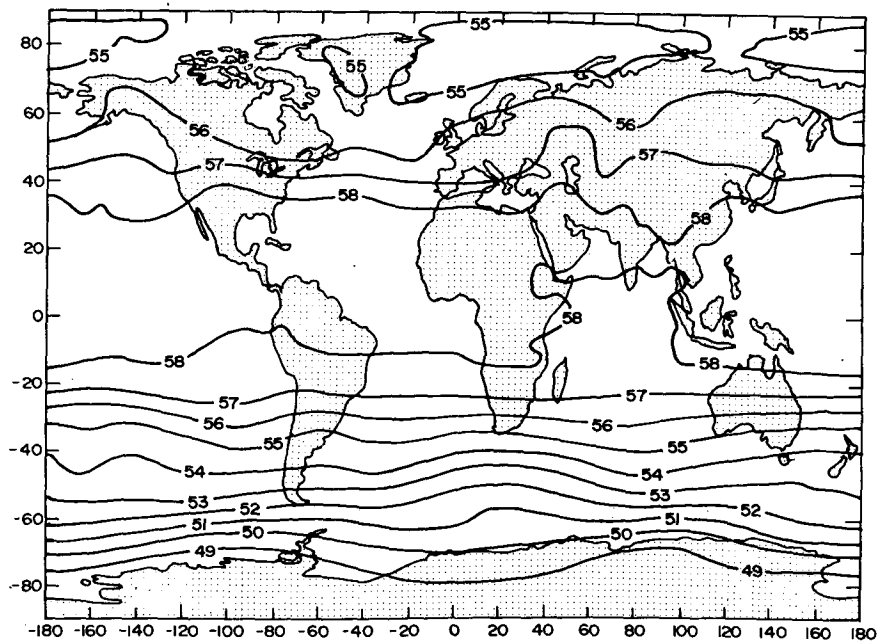
FIG. 4.19. As in Fig. 4.18 except for July.

Ocean in January and in the central Pacific in both seasons to be too near the equator, and to be too far north over Africa in July (Riehl, 1954; Godshall, 1968). The displacement over Africa in July is caused by the ground albedo in the model always being taken to be 0.14. Other studies have shown that a more realistic albedo over the Sahara of 0.35 leads to a correct positioning of the ITCZ over Africa in July (Charney et al., 1975).

Figs. 4.22 and 4.23 show maps of the model-simulated precipitation rates in January and July, respectively. The sampling interval of only 4 h used in calculating the means can cause errors as large as 25% in the precipitation rates at individual grid points. The tropical rainbelt and the subtropical dry belts and their seasonal differences have all been simulated realistically. For example, the rainfall maxima over South America and Africa have shifted northward by about 25° and 30° latitude, respectively, in July compared to January, and the Indian monsoon develops in July. The rainbelt
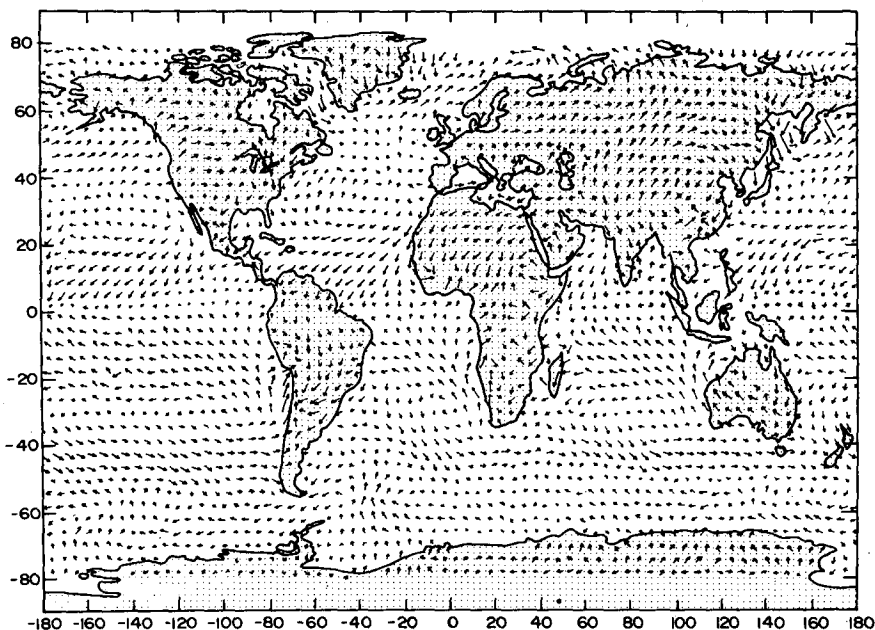


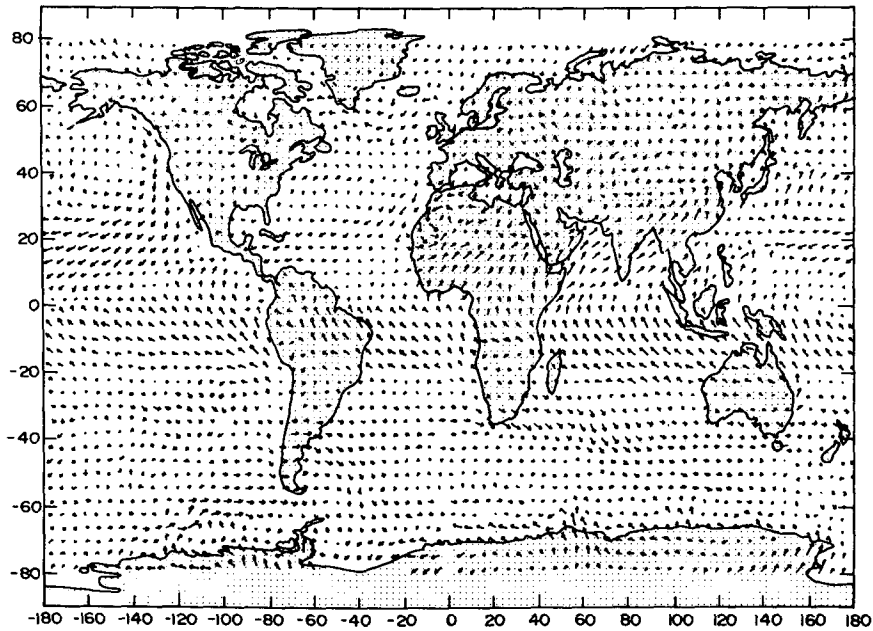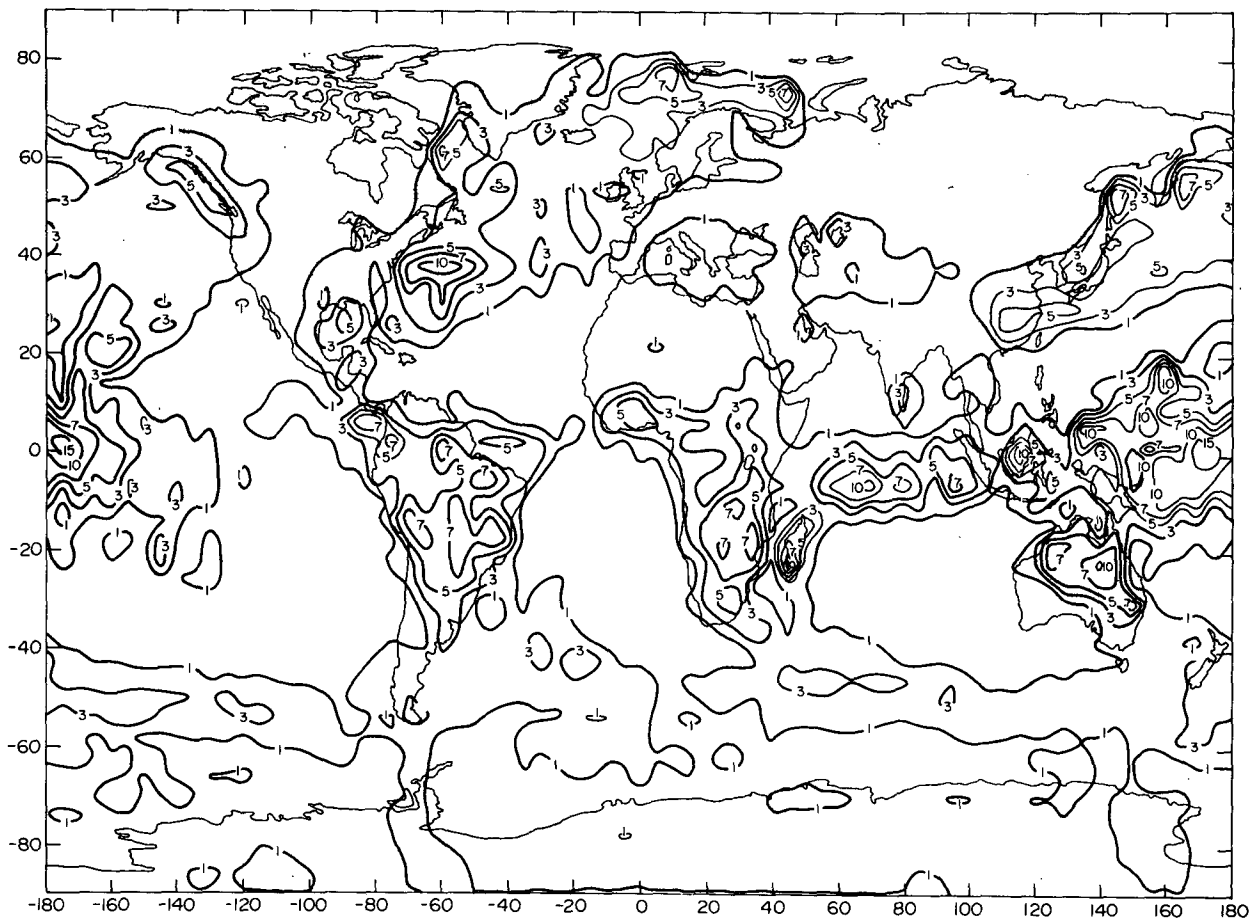FIG. 4.20. Surface wind vectors in the model-simulated January.

FIG. 4.21. As Fig. 4.20 except for July.



FIG. 4.22. Precipitation in mm day$^{-1}$ for the model-simulated January. The precipitation rates have been smoothed with a weighted five-point formula, giving a weight of $\frac{1}{8}$ to the four adjacent points.
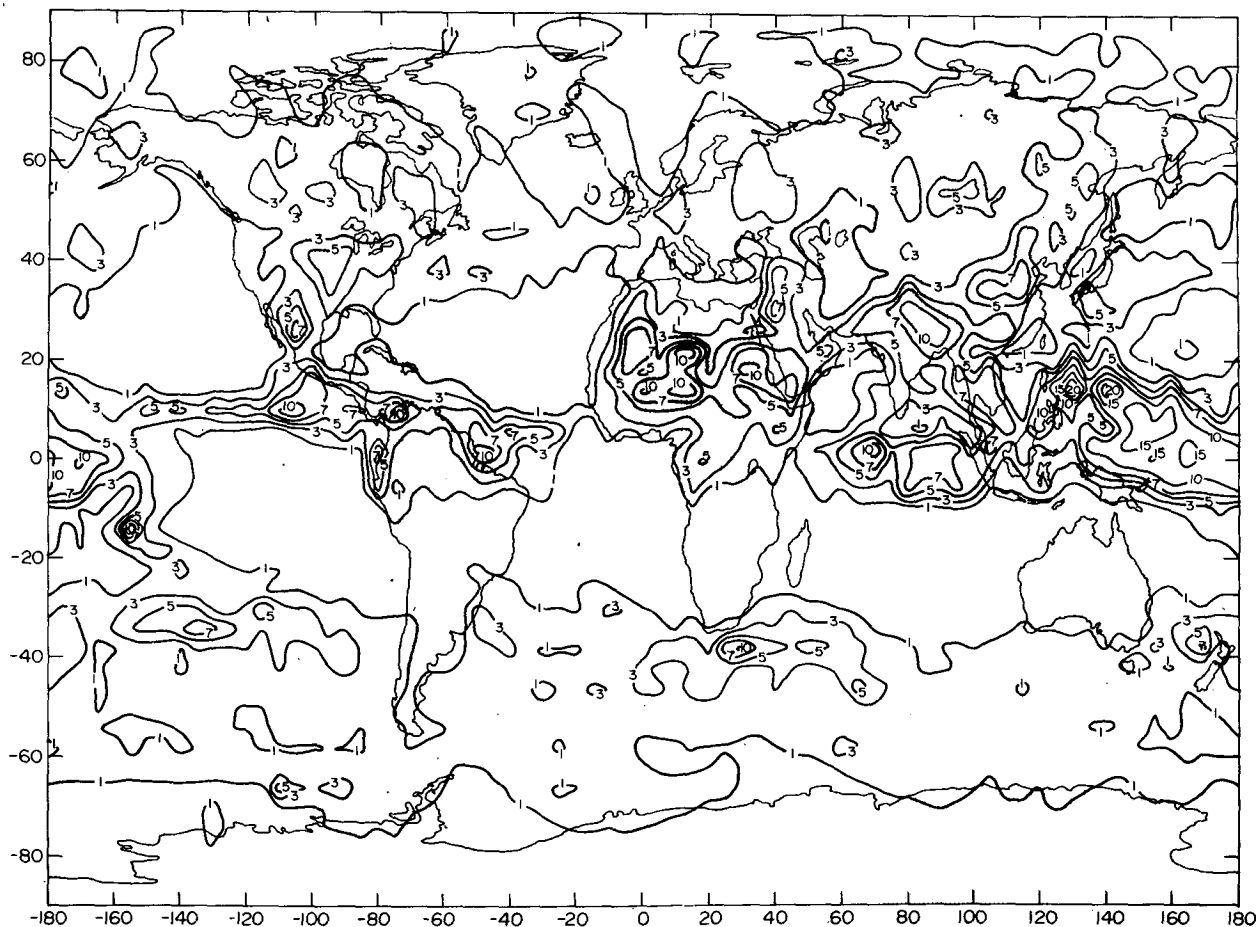
FIG. 4.23. As in Fig. 4.22 except for July.

across Africa in July, like the ITCZ, is actually about 6° latitude too far north (Ramage, 1971). This is partly a result of the unrealistic ground albedo in the Sahara (Charney et al., 1975). The ITCZ shows up particularly clearly in the rainfall pattern over the eastern Pacific in July. The most notable defect in the simulated precipitation rates is their magnitude in July over Southeast Asia, where they are about one-half the observed rate (Ramage, 1971).

## 5. Summary

Atmospheric conditions during the calendar month of July have been simulated with a 44-day integration of the GISS model. The model-generated statistics during the month of July (days 14–44 of the integration) were stable because of the realistic choice of initial conditions. The monthly mean statistics for the July simulation were compared with climatological data, mainly for the Northern Hemisphere troposphere. The comparison shows that the model-generated energy cycle, distribution of winds, temperature, humidity and pressure, dynamical transports, diabatic heating, evaporation, precipitation and cloud cover are all realistic for the Northern Hemisphere troposphere in July.

There are quantitative differences between the model-generated statistics and the climatological data, and these are generally similar to those found in the earlier January simulation (Somerville et al., 1974). In both seasons the simulations tend to underestimate the eddy activity, the strength of the mean meridional circulations, and some of the associated transports. However, the July simulation of the Northern Hemisphere on the whole is superior to the January simulation. In particular, the zonal mean temperature and zonal wind fields are in better agreement with the observed fields. This improvement in the Northern Hemisphere simulation in July appears to be due to the absence of the polar night jet (which cannot be resolved with the model's stratospheric resolution), and to the decreased importance of large-scale dynamical heating and cooling in summer.

The model-simulated seasonal differences determined by comparing the separate January and July simulations, were also evaluated by comparing them with climatological data. The model's simulation of seasonal

differences is generally quite realistic, since the systematic quantitative errors referred to above do not affect the simulation of relative changes, to first order. For example, the northward displacement of the mid-latitude jets, the low-latitude Hadley cells, the tropical rain belt, the trade winds and the ITCZ in July, and the relative decrease in strength of the zonal and meridional circulations and in eddy activity in summer are all in good agreement with the observations. The simulated seasonal variations in the Southern Hemisphere are much smaller than in the Northern Hemisphere.

However, the simulation experiments do reveal three defects that could seriously bias the model's performance in particular climate experiments.

1) The north polar regions are as much as 10 K too cold in January. Errors of this magnitude would place the model at a disadvantage in simulating the amount and extent of polar ice and snow. The albedo of the polar ice and snow supplies a positive feedback to changes in solar radiation and is potentially an important mechanism for modifying climate (Sellers, 1969; Budyko, 1969; Gal-Chen and Schneider, 1976). Improvements in simulating arctic temperatures will require improvements in simulating the dynamical transports. In particular, the eddy flux of sensible heat associated with the Aleutian and Icelandic lows appears to be at fault in the January simulation. The deficiency in the arctic temperatures in January is a common defect in GCM's with resolution comparable to that of the GISS model (Holloway and Manabe, 1971; Kasahara et al., 1973; Newson, 1974).

2) The simulated climate in the vicinity of the Himalayas and Southeast Asia is noticeably poorer than in other areas. For example, the model's simulation of the Siberian High and the low-level winds over the Bay of Bengal, Southeast Asia and the western Pacific in January, and the model's simulation of the Himalayan low and the precipitation rates over Southeast Asia in July are all substandard. The particular importance of topography for the climate of this area, i.e., the Himalayas, suggests that the simulation of topographic effects needs to be improved. Unusual difficulty in simulating the climate in this area is again not unique to the GISS model (Manabe and Holloway, 1975).

3) The global albedo in the July simulation is abnormally high. This defect leads to temperatures which are at most only 2 K too cold, but this temperature error is kept small by the fact that sea surface temperatures were prescribed to have their observed values. In many climate calculations one needs to couple an ocean model to the atmosphere model, and the temperature errors caused by such an albedo error could then be substantially larger. The high albedo in the GISS model is caused at least in part by an excessive frequency of deep convective clouds in July. Correcting this defect will require improvements in the parameterization scheme for moist convection.

REFERENCES

Arakawa, A., 1972: Design of the UCLA atmospheric general circulation model. Tech. Rep. No. 7, Dept. of Meteorology, University of California at Los Angeles.
——, A. Katayama and Y. Mintz, 1969: Numerical simulation of the general circulation of the atmosphere. *Proc. WMO/IUGG Symp. Numerical Weather Prediction,* Tokyo, Japan Meteor. Agency, Vol. 4, Part 7, 8–12.
Budyko, M. I., 1963: *Atlas of the Heat Balance of the Earth.* Moscow, Gidrometeorizdat, 69 pp.
——, 1969: The effect of solar radiation variations on the climate of the earth. *Tellus,* 21, 611–619.
Charney, J., P. H. Stone and W. J. Quirk, 1975: Drought in the Sahara: A biogeophysical feedback mechanism. *Science,* 187, 435–436.
Clapp, P. F., 1964: Global cloud cover for seasons using TIROS nephanalyses. *Mon. Wea. Rev.,* 92, 495–507.
Crutcher, H. L., and J. M. Meserve, 1970: *Selected Level Heights, Temperatures and Dew Points for the Northern Hemisphere.* NAVAIR 50-1C-52, Naval Weather Service Command.
Deardorff, J. W., Empirical dependence of the eddy coefficient for heat upon stability above the lowest 50 m. *J. Appl. Meteor.,* 6, 631–643.
Dopplick, T. G., 1972: Radiative heating of the global atmosphere. *J. Atmos. Sci.,* 29, 1278–1294.
Druyan, L. M., 1974: Short-range forecasts with the GISS model of the global atmosphere. *Mon. Wea. Rev.,* 102, 269–279.
——, R. C. J. Somerville, and W. J. Quirk, 1975: Extended-range forecasts with the GISS model of the global atmosphere. *Mon. Wea. Rev.,* 103, 779–795.
Flattery, T. W., 1971: Spectral models for global analysis and forecasting. Tech. Rep. 242, Air Weather Service, 42–54.
Gal-Chen, T., and S. H. Schneider, 1976: Energy balance climate modeling: comparison of radiative and dynamic feedback mechanisms. *Tellus,* 28, 108–121.
Gates, W. L., 1972: The January global climate simulated by the two-level Mintz-Arakawa model: a comparison with observation. Rep. R-1005-ARPA, The Rand Corporation, Santa Monica, Calif.
——, 1975: The January global climate simulated by a two-level. general circulation model: a comparison with observation *J. Atmos. Sci.,* 32, 449–477.
Godshall, F. A., 1968: Intertropical convergence zone and mean cloud amount in the tropical Pacific Ocean. *Mon. Wea. Rev.,* 96, 172–175.
Gruber, A., 1971: Fluctuations in the position of the ITCZ in the Atlantic and Pacific Oceans. *J. Atmos. Sci.,* 29, 193–197.
Haurwitz, F., and W. R. Kuhn, 1974: The distribution of tropospheric planetary radiation in the Southern Hemisphere. *J. Appl. Meteor.,* 13, 417–429.
Holloway, J. L., Jr., and S. Manabe, 1971: Simulation of climate by a global general circulation model: I. Hydrologic cycle and heat balance. *Mon. Wea. Rev.,* 99, 335–370.
Jastrow, R., and M. Halem, 1973: Simulation studies and the design of the first GARP global experiment. *Bull. Amer. Meteor. Soc.,* 54, 13–21.

Kasahara, A., T. Sasamori and W. Washington, 1973: Simulation experiments with a 12-layer stratospheric global circulation model: I. Dynamical effect of the earth's orography and thermal influence of continentality. *J. Atmos. Sci.*, **30**, 1229–1251.

Kuo, H.-L., 1956: Forced and free meridional circulations in the atmosphere. *J. Meteor.*, **13**, 561–568.

Lacis, A. A., and J. E. Hansen, 1974: A parameterization for the absorption of solar radiation in the earth's atmosphere. *J. Atmos. Sci.*, **31**, 118–133.

Manabe, S., D. G. Hahn and J. L. Holloway, Jr., 1974: The seasonal variation of the tropical circulation as simulated by a global model of the atmosphere. *J. Atmos. Sci.*, **31**, 43–83.

——, and J. L. Holloway, Jr., 1975: The seasonal variation of the hydrologic cycle as simulated by a global model of the atmosphere. *J. Geophys. Res.*, **80**, 1617–1649.

——, J. Smagorinsky, J. L. Holloway, Jr., and H. M. Stone, 1970: Simulated climatology of a general circulation model with hydrologic cycle: III. Effects of increased horizontal computational resolution. *Mon. Wea. Rev.*, **98**, 175–212.

Möller, F., 1951: Vierteljahrskarten des Niederschlags für die ganze Erde. *Petermanns Geogr. Mitt.*, Gotha, Justus Perthes, 1–7.

Newson, R. L., 1974: An experiment with a tropospheric and stratospheric three-dimensional circulation model. *Proc. 3rd Conf. CIAP.* Cambridge, U. S. Dept. of Transportation, 461–473.

Ogura, Y., and H.-R. Cho, 1973: Diagnostic determination of cumulus cloud populations from observed large-scale variables. *J. Atmos. Sci.*, **30**, 1276–1286.

Oort, A. H., 1964: On estimates of the atmospheric energy cycle. *Mon. Wea. Rev.*, **92**, 483–493.

——, and J. P. Peixoto, 1974: The annual cycle of the energetics of the atmosphere on a planetary scale. *J. Geophys. Res.*, **79**, 2705–2719.

——, and E. M. Rasmusson, 1971: *Atmospheric Circulation Statistics.* NOAA Prof. Paper 5.

Peixoto, J. P., and A. H. Oort, 1974: The annual distribution of atmospheric energy on a planetary scale. *J. Geophys. Res.*, **79**, 2149–2159.

Ramage, C. S., 1971: *Monsoon Meteorology.* Academic Press, p. 251.

Riehl, M., 1954: *Tropical Meteorology.* McGraw-Hill, p. 8.

Rodgers, C. D., 1967: The radiative heat budget of the troposphere and lower stratosphere. Rep. A2, Dept. of Meteorology, MIT, 99 pp.

Saltzman, B., 1970: Large-scale atmospheric energetics in the wavenumber domain. *Rev. Geophys. Space Phys.*, **8**, 289–302.

Sasamori, T., J. London and D. V. Hoyt, 1972: Radiation budget of the Southern Hemisphere. *Meteor. Monogr.*, No. 35, 9–23.

Schneider, E. K., and R. S. Lindzen, 1976: A discussion of the parameterization of momentum exchange by cumulus convection. *J. Geophys. Res.*, **81**, 3158–3160.

Schutz, C., and W. L. Gates, 1971: Global climatic data for surface, 800 mb. 400 mb: January. Rep. R-915-ARPA, The Rand Corporation, Santa Monica, Calif.

——, and ——, 1972a: Supplemental global climatic data. January. Rep. R-915/1-ARPA, The Rand Corporation, Santa Monica, Calif.

——, and ——, 1972b: Global climatic data for surface, 800 mb., 400 mb.: July. Rep. R-1029-ARPA, The Rand Corporation, Santa Monica, Calif.

Sellers, W. D., 1969: A global climatic model based on the energy balance of the earth-atmosphere system. *J. Appl. Meteor.*, **8**, 392–400.

SMIC, 1971: *Inadvertent Climate Modification.* Cambridge, The MIT Press, p. 115.

Somerville, R. C. J., W. J. Quirk, J. E. Hansen, A. A. Lacis and P. H. Stone, 1976: A search for short-term meteorological effects of solar variability in an atmospheric circulation model. *J. Geophys. Res.*, **81**, 1572–1576.

——, P. H. Stone, M. Halem, J. E. Hansen, J. S. Hogan, L. M. Druyan, G. Russell, A. A. Lacis, W. J. Quirk and J. Tenenbaum, 1974: The GISS model of the global atmosphere. *J. Atmos. Sci.*, **31**, 84–117.

Stone, P. H., S. Chow, H. M. Helfand, W. J. Quirk and R. C. J. Somerville, 1975: Seasonal changes in the atmospheric heat balance simulated by the GISS general circulation model. *Proc. WMO/IAMAP Symp. Long-Term Climatic Fluctuations,* Geneva, WMO Publ. No. 421, 383–389.

——, W. J. Quirk and R. C. J. Somerville, 1974: The effect of small-scale vertical mixing of horizontal momentum in a general circulation model. *Mon. Wea. Rev.*, **102**, 765–771.

Taljaard, J., H. van Loon, H. Crutcher, and R. Jenne, 1969: *Climate of the Upper-Air: Southern Hemisphere,* Vol. 1. NAVAIR 50-1C-55, Naval Weather Service Command.

Tenenbaum, J., 1976: Spectral and spatial energetics of the GISS model atmosphere. *Mon. Wea. Rev.*, **104**, 15–30.

U. S. Navy Hydrographic Office, 1944: *World Atlas of Sea Surface Temperatures.* H. O. Pub. No. 225.

——, 1957: *Oceanographic Atlas of the Polar Seas:* Part I. *Antarctic.* H. O. Pub. No. 705.

——, 1958: *Oceanographic Atlas of the Polar Seas:* Part II. *Arctic.* H. O. Pub. No. 705.

van Loon, H., 1972: Wind in the Southern Hemisphere. *Meteor. Mono.*, No. 35, 87–100.

Vonder Haar, T. H., and V. E. Suomi, 1971: Measurements of the earth's radiation budget from satellites during a five-year period. Part I: Extended time and space means. *J. Atmos. Sci.*, **28**, 305–314.

Washington, W. M., and L. G. Thiel, 1970: Digitized monthly mean ocean temperatures over the globe. Tech. Note 54, National Center for Atmospheric Research, 30 pp.

Webster, P. J., and J. L. Keller, 1975: Atmospheric variations: vacillations and index cycles. *J. Atmos. Sci.*, **32**, 1283–1300.

Wellck, R. E., A. Kasahara, W. M. Washington and G. Santo, 1971: Effect of horizontal resolution in a finite-difference model of the general circulation. *Mon. Wea. Rev.*, **99**, 673–683.